BubR1 recruitment to the kinetochore via Bub1 enhances Spindle Assembly Checkpoint signaling

Anand Banerjee[1,*, #], Chu Chen[2,*], Lauren Humphrey[2], John J. Tyson[1], Ajit P. Joglekar[2, #]

1 – Academy of Integrated Science, Virginia Polytechnic Institute & State University, Blacksburg, VA 24601, USA

2 – Cell & Developmental Biology, University of Michigan Medical School, Ann Arbor, MI 48109, USA

* - These authors contributed equally.

[#] – corresponding authors

Abstract

During mitosis, unattached kinetochores in a dividing cell generate the anaphase-inhibitory Mitotic Checkpoint Complex (MCC) to activate the Spindle Assembly Checkpoint (SAC) and delay anaphase onset. To generate MCC, these kinetochores recruit MCC constituent proteins including the protein BubR1. The increased local concentration of BubR1 resulting from this recruitment should enhance MCC generation, but prior studies found this not to be the case. We analyzed the contribution of two BubR1 recruitment pathways to MCC generation in human kinetochores. For these analyses, we isolated a subset of the MCC generation reactions to the cytosol using ectopic SAC activation systems. These analyses and mathematical modeling show that BubR1 binding to the SAC protein Bub1, but not to the 'KI' motifs in the kinetochore protein Knl1, significantly enhances the rate of Bub1-mediated MCC generation in the kinetochore. Our work also suggests that Bub1-BubR1 stoichiometry will strongly influence the dose-response characteristics of SAC signaling.

Keywords: mitosis, Spindle Assembly Checkpoint, eSAC, kinetochores, mathematical modeling

Introduction

The “Spindle Assembly Checkpoint” (SAC) is a cell cycle control that minimizes chromosome missegregation during cell division (Musacchio, 2015). It is activated by kinetochores that are not stably attached to the plus-ends of spindle microtubules. These kinetochores generate a diffusible anaphase-inhibitory signal in the form of the Mitotic Checkpoint Complex (MCC), which in turn delays anaphase onset to avert cell division. The amount of MCC in the dividing cell controls the delay in anaphase onset. This amount depends on the number of unattached kinetochores and the rate at which each kinetochore generates MCC (Collin et al., 2013; Dick and Gerlich, 2013). Therefore, the latter parameter is a key determinant of the delay in anaphase onset and chromosome segregation accuracy (Roy et al., 2020).

The rate at which an unattached kinetochore generates MCC depends on its ability to recruit MCC components Mad2, and Cdc20 (Vleugel et al., 2015; Vleugel et al., 2013) (Figure 1A, dashed square). Upon their recruitment to unattached kinetochores, these proteins interact to generate either the MCC itself (or the C-Mad2-Cdc20 subcomplex). Recent discoveries show that Bub1 plays a major role in coordinating the formation of the C-Mad2-Cdc20 subcomplex, which is a crucial, but rate-limiting step in MCC formation (Faesen et al., 2017; Lara-Gonzalez et al., 2021; Piano et al., 2021). Bub1 also heterodimerizes with BubR1 (Overlack et al., 2015). Given this knowledge, it is reasonable to expect that BubR1 recruitment to the kinetochore will increase the rate of MCC generation. Interestingly, however, this expectation does not appear to hold. Disruption of BubR1 recruitment to unattached kinetochores does not reduce the duration of SAC-induced mitotic arrest in nocodazole-treated cells (Overlack et al., 2015; Zhang et al., 2016). This finding is counter-intuitive, because decreased local BubR1 concentration in the kinetochore should reduce the rate of MCC formation by the kinetochore, and therefore lessen the delay in anaphase onset. A possible explanation for this finding is that BubR1 recruits Protein Phosphatase 2A (PP2A) to the kinetochore, which indirectly promotes SAC silencing (Foley et al., 2011; Nijenhuis et al., 2014).

In this study, we re-examine the contribution of kinetochore recruitment of BubR1 to SAC signaling in HeLa cells. To overcome the challenges associated with studying SAC signaling within kinetochores, we use the ectopic SAC activation system or the ‘eSAC’ to isolate specific signaling interactions in the cytosol (Chen et al., 2019). We find that Bub1-BubR1 heterodimerization elevates Bub1-mediated MCC generation. On the other hand, the recruitment of Bub1 and BubR1 via the ‘KI’ motifs in the kinetochore protein Knl1 does not contribute to MCC generation mediated by the MELT motifs within the Knl1 phosphodomain (Bolanos-Garcia et al.,

58 2011a; Bolanos-Garcia et al., 2011b; Kiyomitsu et al., 2011; Krenn et al., 2012; Primorac et al.,
59 2013; Vleugel et al., 2013; Zhang et al., 2014). We also establish a mathematical model to
60 elucidate the mechanistic details of the SAC signaling cascade that generates the MCC. We
61 confirm these findings in the context of kinetochore-based SAC signaling.

62

63 **Results**

64 **The BubR1 binding domain of Bub1 promotes Bub1-mediated MCC assembly**

65 BubR1 is recruited to the human kinetochore by: (1) its heterodimerization with Bub1, which itself
66 binds to the kinetochore protein Knl1 as part of the Bub1-Bub3 complex, and (2) its binding to the
67 'KI motif' located within the N-terminal domain of Knl1 (Figure 1A) (Bolanos-Garcia et al., 2011b;
68 Kiyomitsu et al., 2011; Krenn et al., 2014; Leontiou et al., 2019; Nijenhuis et al., 2013). We first
69 examined whether Bub1-BubR1 heterodimerization contributes to Bub1-mediated MCC
70 assembly. Conventional assays are ill-suited to directly address this question, because both Bub1
71 and BubR1 recruit regulatory enzymes to the kinetochore. Consequently, any disruption of the
72 recruitment of the SAC proteins to the kinetochore is bound to perturb the intricate regulation of
73 signaling activities within the kinetochore. Therefore, we first decided to employ the ectopic SAC
74 activation system (the eSAC) to isolate Bub1-mediated MCC generation in the cytoplasm and
75 then quantitatively dissect the role of Bub1-BubR1 heterodimerization in MCC assembly.

76 We and others have previously found that the induced dimerization of a fragment of the central
77 domain of Bub1 with Mps1 delays anaphase onset in HeLa cells, budding yeast, and fission yeast
78 (Chen et al., 2019; Leontiou et al., 2019; Yuan et al., 2017). In HeLa cells, induced dimerization
79 of the central domain of Bub1 (Bub1$^{231-620}$-mNG-2xFkbp12, diagram in Figure 1B) with the Mps1
80 kinase domain (Frb-mCherry-Mps1$^{500-817}$) produced a dose-dependent delay in anaphase onset
81 with a maximal duration of ~ 145 minutes (Figure 1B replotted for comparison from (Chen et al.,
82 2019)). To test whether Bub1-BubR1 heterodimerization contributes to Bub1-mediated MCC
83 assembly, we performed dose-response analysis on a truncated Bub1 phosphodomain that lacks
84 the BubR1 heterodimerization domain (Bub1$^{444-620}$-mNG-2xFkbp12) (Overlack et al., 2015).
85 Ectopic SAC activation using this truncated Bub1 phosphodomain elicited a significantly weaker
86 response, with a maximal mitotic duration of ~ 105 minutes (Figure 1C, plateau of the 4-parameter
87 sigmoid predicted as 105 ± 6 minutes, the range indicates 95% confidence intervals, see Materials
88 and Methods for details). It should be noted that the removal of the Bub3-binding GLEBS domain
89 in the truncated phosphodomain is not responsible for the observed decrease in the maximal

mitotic delay induced by the eSAC activity (Roy et al., 2021). Thus, Bub1-BubR1 heterodimerization contributes to the ability of the Bub1 phosphodomain to generate MCC. A similar observation was reported by a recent *in vitro* study (Piano et al., 2021).

To understand whether a mechanism based on local BubR1 enrichment can explain the dose-response data, we constructed a numerical model that simulates key steps in MCC generation by the eSAC system and the effect of this MCC on the metaphase-to-anaphase transition (see Materials and Methods). This model consists of two stages. In the first stage, we calculate the equilibrium concentrations of two types of signaling complexes that the Bub1 phosphodomain ($Bub1^{231\text{-}620}$) can form: one that contains both BubR1 and Mad1 and one containing only Mad1 (Figure 1D, left; phosphodomains that do not bind Mad1 cannot generate MCC). BubR1 interacts with the Bub1 phosphodomain regardless of its phosphorylation state, whereas Mad1 interacts only with the phosphorylated phosphodomain (Faesen et al., 2017; Ji et al., 2017). Therefore, the latter interaction depends on the amount of Frb-mCherry-$Mps1^{500\text{-}817}$, i.e., the eSAC dosage. We assume that the cellular concentration of the eSAC phosphodomain is higher than both BubR1 and Mad1 concentration (this is experimentally confirmed later). Consequently, the number of signaling complexes saturates at high eSAC dosage (Figure S1A). Cdc20 recruitment to either signaling complex is assumed to be independent of phosphorylation as well as BubR1 or Mad1 binding to the phosphodomain (not depicted).

The signaling complex containing Bub1, BubR1, Mad1, and Cdc20 facilitates the formation of either the Mad2-Cdc20 complex or the MCC. Since the rate-limiting step in MCC assembly is the formation of Mad2-Cdc20, we choose the same rate constant for the formation of MCC and Mad2-Cdc20 (Faesen et al., 2017). We assume that a newly formed Mad2-Cdc20 at the phosphodomain can combine with BubR1 to form the MCC with probability p, or escape to the cytoplasm with probability $1-p$. Thus, the rates of MCC and Mad2-Cdc20 formation at the Bub1 phosphodomain are given by:

$$\text{MCC formation rate at Bub1}^{231\text{-}620} = p \cdot k_{\text{asmcc2}} \cdot [\text{Mad2}]_{\text{I}} \cdot [\text{Cdc20-Bub1-BubR1}]$$

$$\text{Mad2-Cdc20 formation rate at Bub1}^{231\text{-}620}\text{or Bub1}^{444\text{-}620}$$
$$= (1-p) \cdot k_{\text{asmcc2}} \cdot [\text{Mad2}]_{\text{I}} \cdot [\text{Cdc20-Bub1-BubR1}],$$

where $[\text{Mad2}]_{\text{I}}$ is the concentration of inactive (open) form of Mad2 in the cytoplasm and [Cdc20-Bub1-BubR1] is the concentration of the complex between Bub1, BubR1, and Cdc20. This simplified reaction scheme assumes MCC formation to be a one-step reaction.

121 The important question is whether Bub1-BubR1 heterodimerization promotes MCC formation at
122 the Bub1 phosphodomain. If we assume that it does not contribute to MCC formation (or in the
123 case of Bub1$^{444\text{-}620}$, which lacks the BubR1 binding site), then only Mad2-Cdc20 will be produced
124 at the phosphodomain. This sub-complex must interact with BubR1 in the cytosol to complete
125 MCC formation. We calculate this rate as:

126 $$\text{MCC formation rate in the cytoplsam} = k_{\text{asmcc1}} \cdot [\text{BubR1}]_{\text{f}} \cdot [\text{Mad2-Cdc20}],$$

127 where $[\text{BubR1}]_{\text{f}}$ is the concentration of free BubR1 in the cytoplasm. To simulate the effect of
128 MCC generation by these two mechanisms on mitotic progression, we modified a previously
129 described model of the metaphase-to-anaphase transition (Chen et al., 2019; He et al., 2011)
130 (Methods, also see Figure S1B).

131 We first simulated the dose-response curve for Bub1$^{444\text{-}620}$ by assuming a suitable value for the
132 k_{asmcc1} parameter (assumed protein concentrations and rate constants are listed in Table S1).
133 Next, we simulated dose-response data for Bub1$^{231\text{-}620}$. When we assumed that BubR1 binding to
134 the kinetochore does not affect the rate of MCC generation, i.e., $p = 0$ in the above equations,
135 the simulation generated a weaker dose-response curve with a lower maximal response (dotted
136 blue line in Figure 1E). The response is weaker because BubR1 bound to Bub1 cannot participate
137 in cytosolic MCC assembly, and consequently, the rate of cytoplasmic MCC generation is
138 reduced. This result is inconsistent with the observed dose-response curves. The nominal choice
139 of $p = 1$ and $k_{\text{asmcc2}} = 0.5\ \text{nM}^{-1}\text{min}^{-1}$ resulted in longer delays in anaphase onset - matching
140 the observed maximal response (Cyclin B dynamics shown in Figure S1C).

141 A comparison of the total MCC formation rates according to Eq. 1 and 2 shows that the cumulative
142 MCC formation rate is only modestly higher (~ 12%) when the BubR1 heterodimerization domain
143 is present in the phosphodomain (Figure S1D). However, this cumulative rate includes
144 contributions from both types of signaling complexes present in the cell. We wanted to assess the
145 magnitude of enhancement in MCC generation for each signaling complex. To roughly estimate
146 this local speed-up, we first observe that, in the case of a full Bub1 phosphodomain, the rate of
147 MCC formation is proportional to the concentration of Bub1-Cdc20-BubR1 (Figure S1E left).
148 Similarly, in the case of Bub1$^{444\text{-}620}$, the rate of MCC assembly in the cytoplasm is roughly
149 proportional to the Bub1-Cdc20 complex concentration (this complex must bind BubR1 in the
150 cytoplasm to complete MCC assembly, Figure S1E right). Therefore, upon taking the ratio of the
151 concentrations of these two complexes, we find that the rate of MCC assembly per
152 phosphodomain due to Bub1-Cdc20-BubR1 complex is ~ 10 times faster than the effective rate

153 of MCC assembly due to Bub1-Cdc20 complex (note the difference in the scaling factors used to
154 display the concentrations of the two complexes in Figure S1E).

155

156 **KI motifs suppress the signaling strength of the eSAC phosphodomain**

157 The KI motifs, so named because of the critical role that Lysine and iso-Leucine residues play in
158 their activities, also recruit Bub1 and BubR1 to the human kinetochore (Figure 1A). The first KI
159 motif (KI1) is thought to exclusively bind Bub1, whereas the second motif (KI2) is thought to bind
160 BubR1 (Krenn et al., 2012). A prior study concluded that the KI motifs cooperate with the first
161 MELT motif in KNL1 to strengthen SAC signaling (Krenn et al., 2014). However, it is unclear
162 whether this is because Bub1 and BubR1 recruited by the KI motifs participate in MCC assembly
163 or because they recruit regulatory enzymes (e.g., PLK1, PP2A) that promote SAC signaling
164 (Nijenhuis et al., 2014). Therefore, to test whether Bub1 and BubR1 bound to the KI motifs directly
165 promote MCC assembly and to delineate the roles of the two KI motifs, we developed another
166 eSAC system. In this system, a fragment of Knl1 spanning the first MELT motif and the two KI
167 motifs serves as the phosphodomain (Knl1$^{160\text{-}256}$, Figure 2A). Additionally, we created a variant
168 phosphodomain wherein the two KI motifs are inactivated by mutating the residues identified as
169 critical for their activity (Krenn et al., 2012). If Bub1 and BubR1 recruitment via the KI motifs
170 enhances MELT motif activity, this will be apparent as increased signaling strength of the eSAC
171 phosphodomain.

172 To establish the basal activity of the first MELT motif, we first studied the dependence of mitotic
173 duration on the dosage of the eSAC signaling complex consisting of the eSAC phosphodomain
174 with mutant, inactive KI motifs (M1-KI1*-KI2*-mNG-2xFkbp12, Figure 2A left). As before, the data
175 was fit with a sigmoidal curve (Figure 2A, middle panel) (Chen et al., 2019). The maximal
176 response for this phosphodomain was higher than the previously defined maximal response for
177 the eSAC phosphodomain containing the 12th MELT motif (211 versus 157 minutes with ± 95%
178 confidence intervals of 169-357 and 152-163 respectively predicted by a 4-parameter sigmoidal
179 fit to the binned data). This difference likely reflects the difference in the Bub1-Bub3 binding
180 affinities of the first and twelfth MELT motif (Vleugel et al., 2015). Interestingly, the inclusion of
181 active KI motifs in the phosphodomain significantly depressed its signaling strength: the eSAC
182 concentration required for half-maximal response nearly doubled (EC50 = 9.7 and 19.4 a. u.
183 respectively, Figure 2A middle). Decrease in the apparent signaling strength of the
184 phosphodomain was eventually compensated by high eSAC dosage, and therefore, the maximal
185 response was similar in value (Figure 2A middle and right).

186 Thus, the inclusion of the KI motifs in the eSAC phosphodomain suppressed MCC production
187 mediated by the phosphorylated MELT motif within the same phosphodomain. Our eSAC-based
188 analyses of the Bub1 phosphodomain in the prior section provides a possible explanation for this
189 unexpected observation: if one assumes that the KI motifs interact with Bub1 and BubR1
190 independently of the MELT motif, and if the Bub1 and BubR1 molecules recruited by the KI motifs
191 do not participate in MCC formation mediated by the MELT motif, then the KI motifs will effectively
192 sequester Bub1 and BubR1 from MELT-motif mediated MCC assembly. This will suppress the
193 signaling activity of the eSAC.

194

195 **Bub1 and BubR1 interactions with the KI motifs do not require Mps1-mediated**
196 **phosphorylation of KNL1; Bub1 interacts with both KI motifs**

197 To delineate the activities of the KI motifs in the eSAC system, we constructed a new
198 phosphodomain by fusing an unstructured region of the Knl1 phosphodomain spanning three
199 previously characterized MELT motifs (Knl1$^{881-1014}$) to the C-terminus of the phosphodomain used
200 above (Knl1$^{160-256}$, see Figure 2B) (Chen et al., 2019; Vleugel et al., 2015). We also created mutant
201 versions of this phosphodomain wherein the KI motifs were rendered inactive either individually
202 or together using point mutations (KI1*-KI2, KI1-KI2*, and KI1*-KI2* with the asterisk denoting
203 loss of activity, Figure 2B) (Krenn et al., 2012). By incorporating multiple MELT motifs in the
204 phosphodomain, we wanted to test whether the KI motifs influence the ability of the four MELT
205 motifs in the phosphodomain to engage in synergistic signaling (Chen et al., 2019).

206 We first determined whether the two KI motifs interact with Bub1 and BubR1 exclusively, and
207 whether MELT motif phosphorylation is necessary for these interactions. We immunoprecipitated
208 the four, mNeonGreen-tagged eSAC phosphodomains from whole cell extracts of mitotic HeLa
209 cells in the absence of the Mps1 kinase domain using mNeonTrap beads and probed the
210 precipitates for Bub1 and BubR1 (Methods). When both KI motifs were active (KI1-KI2), Bub1
211 and BubR1 co-precipitated with the eSAC phosphodomain. When both KI motifs were inactive
212 (KI1*-KI2*), Bub1 and BubR1 did not co-precipitate with the eSAC phosphodomain as expected
213 (Figure 2B). Surprisingly, when the first KI motif, which is expected to interact with Bub1 alone,
214 was inactive (KI1*-KI2), Bub1 still co-precipitated with the phosphodomain albeit at a lower level.
215 BubR1 coprecipitation was also reduced. This observation suggests that Bub1 competes with
216 BubR1 to bind to the second KI motif. Consistent with this inference, inactivation of second KI
217 motif (KI1-KI2*) made BubR1 undetectable in the precipitate and reduced the amount of Bub1.

218 We obtained similar results from immunoprecipitation experiments involving eSAC
219 phosphodomains with only one MELT motif and the two KI motifs (Supplementary Figure S2A).
220 These results show that the first KI motif binds only Bub1, but the second motif can bind Bub1 or
221 BubR1. Furthermore, these interactions are not dependent on MELT motif phosphorylation.

222

223 **Bub1 and BubR1 recruited by the KI motifs do not contribute to MCC assembly mediated**
224 **by the MELT motifs**

225 Having established the biochemical activities of the KI motifs, we performed dose-response
226 analysis for the eSAC phosphodomain containing inactive KI motifs to define the baseline activity
227 of the four MELT motifs (KI1*-KI2* in Figure 2B left, purple circles). The response elicited by the
228 eSAC phosphodomain with four MELT motifs to increasing eSAC concentration was non-
229 monotonic and characterized by an initial steep rise that is followed by a gradual decay in the
230 mitotic duration (residuals from a sigmoidal fit to the dose-response data points is shown in Figure
231 S2B, left). It should be noted that such non-monotonic response was not observed for a previously
232 characterized eSAC phosphodomain also containing four MELT motifs (numbers 11-14) (Chen et
233 al., 2019). The different behaviors of the two phosphodomains may be due to a higher affinity of
234 the 1st MELT motif compared to the 11th MELT motif for binding Bub3-Bub1 (Vleugel et al., 2015).
235 Interestingly, when both KI motifs were active, the maximal duration of mitosis was significantly
236 reduced (~ 87 minutes estimated by 4-parameter sigmoidal fit to the binned averages of the data,
237 see Figure 2C). Qualitatively similar results were obtained for an extended phosphodomain
238 containing 7 MELT motifs and the two KI motifs (Figure S2C).

239 We next determined the dose-response dependence for two eSAC phosphodomains containing
240 four MELT motifs and only one active KI motif. When only the first KI motif was active (KI1-KI2*,
241 only Bub1 depleted, see Figure 2B), the dose-response data were monotonic with a slightly lower
242 maximal response (Figure 2C green circles and curve). When only the second KI motif was active
243 (KI1*-KI2, Bub1 and BubR1 depleted, Figure 2C), the maximal response was significantly
244 attenuated (blue circles and line in Figure 2C). Interestingly, the response to this eSAC was non-
245 monotonic: an initial overshoot was followed by decay to a lower maximal response (residuals
246 from the sigmoidal fit in Figure S2B, right). These results further show that Bub1 and BubR1
247 recruited by the two KI motifs do not directly contribute to MCC generation by the MELT motifs
248 within the same phosphodomain in the eSAC system (Figure 2C). The likely explanation for the
249 suppression of eSAC signaling activity is that Bub1 and BubR1 recruitment by the KI motifs
250 sequesters these proteins preventing them from participating in eSAC signaling.

251 One simple explanation for the strong suppression of eSAC signaling activity by the second KI
252 motif is that this motif sequesters BubR1 along with Bub1. Since BubR1 is an MCC component,
253 its sequestration will limit the maximal amount of MCC (MCC_{max}) that the eSAC can generate.
254 Although we could not quantify the amount of MCC produced by the eSAC, this amount and
255 MCC_{max} can both be compared qualitatively by studying the duration of mitotic delays. The eSAC
256 systems discussed here delay mitosis by at most 300 minutes. In contrast, RPE-1 cells treated
257 with high doses of nocodazole arrest for ~ 1500 minutes on average (Collin et al., 2013; Dick and
258 Gerlich, 2013). The significantly smaller delay caused by eSAC signaling, when compared to the
259 delay induced by nocodazole treatment, suggests that the eSAC produces MCC levels smaller
260 than MCC_{max} (Dick and Gerlich, 2013). Therefore, a reduced MCC_{max} due to BubR1 sequestration
261 by the second KI motif alone cannot explain the weaker signaling activity.

262

263 **Numerical simulation of the dose-response data**

264 We returned to numerical simulations to understand the mechanistic underpinnings of the dose-
265 response data. The suppression of eSAC signaling activity by the KI motifs is in part because the
266 eSAC phosphodomains are significantly more abundant than Bub1 and BubR1 (shown later).
267 Nonetheless, the quantitative dose-response data provided us with an excellent opportunity to
268 delineate the contribution of BubR1 recruitment at the MELT motifs to MCC formation. Bub1 and
269 BubR1 sequestration will differentially affect the composition of the two signaling complexes:
270 MELpT-Bub1 and MELpT-Bub1-BubR1 that the eSAC phosphodomains can assemble. If these
271 signaling complexes assemble the MCC at different rates, their effects on mitotic progression will
272 also be different (Dick and Gerlich, 2013). Using simulations, we wanted to understand the
273 mechanisms that give rise to the ~ 1.75-fold difference in the maximal mitotic delay generated by
274 KI1-KI2* and KI1*-KI2 (Figure 2C).

275 To understand underlying mechanisms, it is necessary to consider: (a) the effects of the
276 differential sequestration of Bub1 and BubR1 by the two KI motifs on the concentrations of the
277 two signaling complexes, and (b) the rates at which these signaling complexes generate MCC.
278 Both types of signaling complexes will form on the eSAC phosphodomain, because we have
279 previously shown the eSAC phosphodomain recruits Bub1, BubR1, and Mad1 only in cells treated
280 with rapamycin (Chen et al., 2019). The stoichiometry of these two signaling complexes depends
281 on the interplay of two sets of parameters: (1) the stoichiometry of Bub1, BubR1, and the eSAC
282 phosphodomain (quantification presented after the simulations), and (2) the relative affinities of

283 Bub1 and BubR1 for the two KI motifs, of Bub1 for phosphorylated MELT motifs, and of BubR1
284 for Bub1, which are known (Krenn et al., 2014; Vleugel et al., 2015; Zhang et al., 2016).

285 To simulate the activities of the KI motifs, we added two new elements to our previously described
286 model of the eSAC (Chen et al., 2019): the two KI motifs, and the factors Bub1 and BubR1
287 representing Bub1-Bub3 and BubR1-Bub3 respectively (Figure 3A). As before, all interactions are
288 described by mass action kinetics. In accord with our IP results (Figure 2), the model assumes
289 that the first KI motif (KI1) interacts only with Bub1, whereas the second KI motif (KI2) can interact
290 with either Bub1 or BubR1. Based on prior observations, we also assume that only BubR1-Bub3
291 is recruited by the Bub1 bound to a phosphorylated MELT motif (Overlack et al., 2017; Overlack
292 et al., 2015). Based on *in vitro* data, the dissociation constant for Bub1 and BubR1 bound to the
293 KI motifs was assumed to be 6 to 50-fold higher relative to the dissociation constant for Bub1
294 bound to a phosphorylated MELT motif (Chen et al., 2019; Krenn et al., 2012; Overlack et al.,
295 2015; Primorac et al., 2013) (rate constants tabulated in Table S2). We assume that the KI motifs
296 and phosphorylated MELT motifs recruit Bub1 and BubR1 independently. Finally, we also assume
297 that Bub1 and BubR1 bound to the KI motifs do not participate in the signaling events mediated
298 by the phosphorylated MELT motifs (Figure 3A). Three of the four MELT motifs used in the eSAC
299 phosphodomain were used in our previous study. Therefore, their affinities for Bub1 were similar
300 to the values used in the original simulation (Chen et al., 2019). The rate constants for the first,
301 12th and 14th MELT motifs were set to reflect that they have a higher affinity for Bub1 compared
302 to the weaker 13th MELT motif (Vleugel et al., 2015). The protein concentrations used are
303 tabulated in Table S2.

304

305 **Effects of the differential activity of the KI motifs on the distribution of the signaling**
306 **complexes formed by the eSAC phosphodomains**

307 We first calculated the steady-state concentrations of MELpT-Bub1 and MELpT-Bub1-BubR1
308 assembled by KI1-KI2* and KI1*-KI2. Bub1-BubR1 stoichiometry plays a critical role in
309 determining these concentrations. If Bub1-BubR1 stoichiometry is high, e.g., 1:4, nearly every
310 MELpT-Bub1 complex assembled by KI1-KI2* and KI1*-KI2 will recruit BubR1 to form MELpT-
311 Bub1-BubR1 despite the differential depletion of Bub1 and BubR1 by the two phosphodomains
312 (converging dashed lines at high eSAC dosage in Figure 3B, right). Consequently, the
313 concentration of MELpT-Bub1 is negligible (dashed green and blue lines respectively near the X
314 axis in Figure 3B, left). At high eSAC dosage, both KI1-KI2* and KI1*-KI2 form the same signaling
315 complex (MELpT-Bub1-BubR1). Because both phosphodomains form similar amounts of the

316 same signaling complex, they will generate similar amounts of MCC, and therefore produce
317 mitotic delays of similar magnitude.

318 This picture changes when Bub1-BubR1 stoichiometry is around 1:1. In this case, KI1-KI2* and
319 KI1*-KI2 phosphodomains assemble different equilibrium concentrations of MELpT-Bub1 and
320 MELpT-Bub1-BubR1 especially at high eSAC dosage. BubR1 depletion by KI1*-KI2 lowers the
321 amount of MELpT-Bub1-BubR1 that it forms compared to KI1-KI2* (Figure 3B, right, solid lines).
322 Conversely, the concentration of MELpT-Bub1 formed by KI1*-KI2 is now higher, because BubR1
323 availability is reduced (solid lines in Figure 3B, left). Figure 3C shows how Bub1-BubR1
324 stoichiometry affects MELpT-Bub1-BubR1 concentration (Figure 3C left, for the high and constant
325 eSAC dosage = 20). These calculations show that if the KI1-KI2* and KI1*-KI2 phosphodomains
326 are to exhibit different dose-response characteristics, BubR1 (i.e., BubR1-Bub3) cannot be in too
327 much excess of Bub1 (i.e., Bub1-Bub3). Equal Bub1 and BubR1 abundance will produce the
328 maximal difference in the levels of signaling complexes assembled by KI1-KI2* and KI1*-KI2 at
329 high eSAC dosage. This difference in the composition of the signaling complexes can provide the
330 basis for the differential activity of the KI1-KI2* and KI1*-KI2 phosphodomains.

331

332 **A higher rate of MCC generation by MELpT-Bub1-BubR1 compared to MELpT-Bub1 can**
333 **explain the differential behavior of the two phosphodomains**

334 Differences in the maximal concentrations of the MELpT-Bub1 and MELpT-Bub1-BubR1 will
335 translate into different levels of MCC only if they generate MCC at different rates (the ratio of
336 maximal mitotic duration achieved by KI1-KI2* and KI1*-KI2 is indicated by the red horizontal line
337 in Figure 3C). Specifically, MELpT-Bub1-BubR1 must generate MCC at a higher rate than
338 MELpT-Bub1. To simulate MCC generation by the two signaling complexes, we used a simplified
339 process of MCC generation wherein we do not explicitly include the dynamics of Mad2, Bub1 and
340 BubR1. Instead, a single reaction between the signaling complex and free cytoplasmic Cdc20
341 generates MCC, with the forward rate constants k_{MCC} for MELpT-Bub1 and k'_{MCC} for MELpT-Bub1-
342 BubR1 as the only parameters. This simplified, coarse-grained scheme is justified because, the
343 rate of MCC generation at the phosphodomain and in the cytoplasm will be proportional to the
344 concentration of the corresponding signaling complex (see Figure S1E). To simulate the effect of
345 the MCC generated in this manner on mitotic progression, we suitably modified the model of
346 metaphase-to-anaphase transition described by He et al. to reflect the simplified MCC generation
347 scheme (Figure S3B) (Chen et al., 2019; He et al., 2011).

348 To study how k_{MCC} and k'_{MCC} affect the maximal mitotic duration, we fixed the eSAC dosage at a
349 high and constant value, and then calculated the ratio of maximal mitotic duration produced by
350 KI1-KI2* over that produced by KI1*-KI2 as a function of Bub1-BubR1 stoichiometry and
351 k'_{MCC}:k_{MCC} ratio (contour plot in Figure 3D). From this plot we see that the simulations of the ratio
352 of maximal mitotic durations for KI1-KI2* and KI1*-KI2 is 1.4 (close to the observed ratio of ~
353 1.75), when (1) BubR1-Bub1 stoichiometry is ~ 1, and (2) the signaling strength of the MELpT-
354 Bub1-BubR1 signaling complex is at least 6-fold higher than the signaling strength of the MELpT-
355 Bub1 signaling complex.

356 We used this framework to simulate the dose-response curves for all four phosphodomains. In
357 this simulation, we assumed [Bub1]:[BubR1] = 1 and k_{MCC}:k'_{MCC} = 0.1 (corresponding to a 10-fold
358 increase in MCC generation at the eSAC phosphodomain relative to cytoplasmic MCC
359 generation). With these nominal parameter values, dose-response curves generated by the model
360 capture key characteristics of the dose-response data (Figure 3E). As before, the assumption of
361 synergistic signaling is necessary to reproduce the non-monotonicity of the dose-response data
362 for the phosphodomain containing four MELT motifs (Chen et al., 2019). Without it, the responses
363 elicited by all phosphodomains become monotonic (Figure S3D). An interesting feature of the
364 observed dose-response data for the KI1*-KI2 phosphodomain is their non-monotonic nature
365 (Figure 2E). Our simulations suggest that this difference arises due to Bub1 sequestration by the
366 KI motif, which in turn suppresses synergistic signaling. Synergistic signaling by MELT motifs
367 requires high occupancy of MELpT motifs by Bub1-BubR1. For this, the binding between MELpT
368 and Bub1 is the necessary first step. In the KI1*-KI2 eSAC, Bub1 is not sequestered as strongly.
369 This allows the assembly of multiple MELpT-Bub1-BubR1 complexes on the same
370 phosphodomain only at low eSAC concentration. Resultant synergistic signaling becomes
371 observable as a peak in the dose-response curve. In the case of the KI1-KI2* eSAC, such
372 synergistic signaling is modulated due to Bub1 sequestration, and cannot be detected. We found
373 that simply increasing the dissociation constant of KI1-Bub1 binding by a factor of two (thereby
374 decreasing Bub1 sequestration) made the dose-response curve for KI1-KI2* eSAC visibly non-
375 monotonic (not shown).

376

377 **Stoichiometry of Bub1, BubR1, Mad1, and the eSAC phosphodomain in HeLa cells**

378 The simulations show that the stoichiometric ratios among Bub1, BubR1, and the eSAC
379 phosphodomain are critical determinants of the behavior of the eSAC systems. To experimentally
380 measure these ratios, we constructed genome-edited HeLa cell lines wherein mNeonGreen

381 (abbreviated as mNG) was fused to the N-terminus of Bub1 and BubR1, and to the C-terminus of
382 Mad1 (see Materials and Methods). In all three cases, we obtained clonal cell lines with partially
383 edited genomes: approximately half of the protein was labeled; the remaining protein fraction was
384 unlabeled (Figure 4A, also see Methods).

385 Using mNG fluorescence quantitation, we found that the abundance of the eSAC phosphodomain
386 containing two active KI motifs and four MELT motifs was 2-4-fold higher than the three SAC
387 proteins in mitotic cells (Figure 4B). The over-abundance of the eSAC phosphodomain relative to
388 Bub1, BubR1, and Mad1, and the constitutive activity of the two KI motifs together support our
389 assumption that the highly expressed eSAC phosphodomains sequester Bub1, BubR1 or both.
390 Moreover, BubR1 is ~ 2-fold more abundant than both Bub1 and Mad1 (Figure 4C). It should be
391 noted that this abundance corresponds to the total BubR1 in a cell including free BubR1-Bub3 as
392 well as BubR1-Bub3 incorporated into MCC (Overlack et al., 2017). The partitioning of BubR1
393 between the BubR1-Bub3 complex and the MCC remains unknown. Therefore, we conclude that
394 the concentration of BubR1-Bub3 available for SAC signaling is less than 2-fold higher than that
395 of Bub1-Bub3. This is consistent with the prediction of our model that the BubR1:Bub1
396 stoichiometry must be near 1:1 for the observed dose-response data for the KI1-KI2* and KI1*-
397 KI2 phosphodomains.

398

399 **Recruitment of BubR1 by BuB1 per se contributes to the signaling strength of the SAC**

400 Observations from the eSAC systems and our numerical simulations forced us to re-examine the
401 role of Bub1-BubR1 heterodimerization in kinetochore-based SAC signaling. Previous studies
402 using the knock-down and rescue approach found that the disruption of Bub1-BubR1
403 heterodimerization increases the SAC strength in nocodazole-treated cells, increasing the
404 duration of mitotic arrest rather than decreasing it (Krenn et al., 2014; Zhang et al., 2016).
405 However, we noted three factors that may have influenced this result. First, the deletion of different
406 segments of BubR1 in the two studies may have resulted in different levels of residual BubR1 at
407 signaling kinetochores. The second factor arises from the loss of the SAC-antagonizing activity
408 of PP2A due to the disruption of BubR1 recruitment to the kinetochore. The kinetochore
409 attachment and regulatory domain (KARD) of BubR1 was either left intact or mutated to eliminate
410 the binding of the PP2A-recruiting subunit B56α, but not necessarily its other isoforms. Most
411 importantly, the mutant BubR1 may have been overexpressed in these experiments. Higher levels
412 of BubR1 in the cytosol will proportionally increase the rate of cytosolic MCC formation, and the
413 increased rate may mask impaired MCC assembly within kinetochores.

414 To account for these three factors, we designed and performed new BubR1 knock-down/rescue
415 experiments. We knocked down endogenous BubR1 in HeLa-A12 using RNA interference and
416 rescued these cells with mNG-BubR1$^{\Delta 665\text{-}682}$ or mNG-BubR1$^{\Delta 432\text{-}484,\ \Delta 665\text{-}682}$. Both lack the KARD to
417 interact with PP2A-B56 (ΔKARD), while mNG-BubR1$^{\Delta 432\text{-}484,\ \Delta 665\text{-}682}$ cannot heterodimerize with
418 Bub1 (ΔHD, ΔKARD). Therefore, mNG-BubR1$^{\Delta 432\text{-}484,\ \Delta 665\text{-}682}$ has nearly undetectable localization
419 at unattached kinetochores (Figure 5A). In these cells, we induced mitotic arrest using nocodazole
420 treatment following the previous studies. Importantly, we used the genome-edited *mNG-BUBR1*
421 HeLa-A12 cells treated with control siRNA and imaged under identical conditions to establish the
422 physiological BubR1expression level. In our analysis of cells expressing the mutant, mNG-tagged
423 BubR1, we only considered those cells exhibiting mNG intensity that is 0.5–2-times the average
424 mNG intensity of mitotic mNG-BubR1 HeLa-A12 cells (because only around half of total BubR1
425 is tagged in the CRISPR-Cas9-edited cell line, Figure 5B, left).

426 We found that in BubR1 knock-down cells rescued with BubR1 lacking the KARD domain arrested
427 for a significantly longer duration as compared to control cells. This is likely due to the loss of
428 PP2A activity from the kinetochores (Saurin et al., 2011). Importantly, cells rescued with BubR1
429 lacking both the KARD domain and the Bub1 heterodimerization domain arrested for a
430 significantly shorter amount of time in comparison (Figure 5B, right). Thus, the recruitment of
431 BubR1 *per se* contributes to the efficient assembly of MCC.

432

433 **Discussion**

434 Unattached kinetochores are poised to assemble the MCC by recruiting its component subunits:
435 BubR1-Bub3, Mad2, and Cdc20. Therefore, it was surprising that the disruption of BubR1
436 recruitment to the kinetochore was found to be unimportant for SAC signaling in nocodazole-
437 treated cells (Overlack et al., 2015; Zhang et al., 2016). We used the eSAC system to isolate a
438 subset of the biochemical reactions in the MCC generation cascade from the kinetochore and
439 analyzed them in the physiological context. These analyses show that Bub1-BubR1
440 heterodimerization significantly enhances the rate of Bub1-mediated MCC assembly. This
441 enhancement may be simply due to enrichment of BubR1 at the site of formation of Mad2-Cdc20
442 (Lara-Gonzalez et al., 2021; Piano et al., 2021), although more complicated mechanisms may
443 also be at work.

444 We also find that Bub1 and BubR1 recruitment via the KI motifs does not contribute to Bub1-
445 mediated MCC assembly. It is important to note that the eSAC signaling complexes contain only
446 one Knl1 phosphodomain in contrast to the spatially clustered organization of many Knl1
447 phosphodomains within the kinetochore. Therefore, it remains possible that KI motifs directly or
448 indirectly prime SAC signaling by constitutively recruiting Bub1 and BubR1 (Jia et al., 2016; Krenn
449 et al., 2014). Nonetheless, because of the higher affinity of phosphorylated MELT motifs for Bub1-
450 Bub3 and their superior numbers (~ 19 MELT motifs versus 1 KI motif each per Knl1), the MELT
451 motifs will take over Bub1 and BubR1 recruitment once Mps1 becomes fully active within
452 unattached kinetochores. KI motif activity is unlikely to contribute significantly under this condition.

453 We also constructed a numerical model to simulate the dose-response data using experimental
454 data wherever possible and assuming plausible parameter values when data were unavailable.
455 This simple model based on differential sequestration of Bub1 and BubR1 can simulate key
456 features of the dose-response data. The simulations support the following main conclusions. First,
457 Bub1-BubR1 heterodimerization significantly elevates the rate of Bub1-mediated MCC
458 generation. To simulate the observed dose-response data, the rate of MCC assembly due to
459 Bub1-bound BubR1 was assumed to be 10-fold higher when compared to cytoplasmic MCC
460 assembly in our model. This enhanced MCC generation rate is reasonable given that the local
461 concentration of BubR1 will increase by orders of magnitude upon its binding to Bub1, the site
462 where Mad2-Cdc20 is formed. Second, our model further supports the observation that Bub1 and
463 BubR1 recruited by the KI motifs do not contribute to MCC generation. Third, the stoichiometry of
464 Bub1 and BubR1 emerges as a key parameter influencing how the MCC generation output of
465 each kinetochore will change as a function of the number of signaling kinetochores in the cell.
466 These simulations thus establish a useful platform for future studies of SAC signaling.

467 Human kinetochores also use the RZZ pathway to promote MCC assembly, and this pathway can
468 compensate for a partial loss of Bub1 from the kinetochore (Qian et al., 2017; Silio et al., 2015;
469 Zhang et al., 2015). Nevertheless, MELT motif and Bub1-mediated MCC assembly is likely to be
470 critical over the course of a normal cell division. Bub1-mediated recruitment of BubR1 to the
471 kinetochore is especially important because this will significantly enhance the rate of MCC
472 generation within the kinetochore, unlike the RZZ pathway, which likely generates only Mad2-
473 Cdc20 and relies on cytosolic assembly of the MCC. Our study does not clarify the role of the KI
474 motifs. The possibilities include the 'priming' of SAC signaling in the early stages of mitosis by
475 enhancing local Bub1 and BubR1 concentration and the recruitment of regulatory factors via Bub1
476 and BubR1 for kinetochore functions unrelated to SAC signaling.

Acknowledgements

We would like to thank Dr. Stephen S. Taylor for the generous gift of antibodies, Dr. Eugene Makeyev for the HeLa acceptor cell line, and Dr. Michael Lampson for plasmids used in this study. We also thank members of the Joglekar lab for stimulating discussions. Use of the Incucyte system was made possible by a generous gift from the Richard Tam Foundation to Prof. Sue O'Shea (Cell & Developmental Biology, University of Michigan Medical School).

The authors declare that no competing financial interests exist.

487 **Materials and Methods**

488 **Plasmid construction**

489 The plasmids used for the stable cell lines were based on plasmids that have been described
490 previously (Chen et al., 2019). Briefly, the phosphodomain was integrated either *Not*I or *Asc*I and
491 *Xho*I restriction sites to create constitutively expressed phosphodomain-mNeonGreen-2xFkbp12.
492 A Mps1$^{500-857}$ fragment corresponding to the Mps1 kinase domain was integrated into the *Fse*I
493 and *Bgl*II restriction sites to create conditionally expressed Frb-mCherry-Mps1$^{500-857}$.
494 eSAC phosphodomains spanning the 1st MELT motif (M1) and the two KI motifs were created by
495 fusing Knl1$^{160-256}$ to mNeonGreen-2xFkbp12. eSAC phosphodomains containing four MELT
496 motifs and the two KI motifs were created by fusing Knl1$^{160-256}$ to Knl1 fragment Knl1$^{881-1014}$
497 spanning MELT motifs 12-14, which has been characterized previously (Vleugel et al., 2015). The
498 activity of the first KI motif was disrupted by changing its amino acid sequence from
499 'K**I**D**TT**S**F**LANLK' to 'KADAASALANLK' (KI1*). Similarly, the activity of the second KI motif was
500 disrupted by mutating its amino acid sequence from 'KIDFND**F**IK**R**LK' to 'KIDFNDAIKALK' (KI2*)
501 following (Krenn et al., 2012).
502 DNA repair templates used for CRISPR/Cas9 mediated genome editing were constructed via
503 DNA assembly using the NEB HiFi DNA assembly kit as per manufacturer's instructions.
504 Successfully edited alleles encode mNeonGreen-tagged SAC proteins that separate the
505 corresponding wildtype protein and the fluorescent protein mNeonGreen by a short flexible linker
506 (mNG-BUBR1 and mNG-BUB1: GSGGSG; MAD1-mNG: GGAGGSGG). The sequences of all
507 homology-directed repair template plasmids and Cre-Lox recombination-mediated cassette
508 exchange plasmids are available upon request.
509

510 **Tissue culture and cell line construction for eSAC analyses**

511 Henrietta Lacks (HeLa) cells were grown in DMEM media supplemented with 10% FBS, 1%
512 Pen/Strep, 1x-Glutamax, and 25 mM HEPES under standard tissue culture conditions (37 °C and
513 5% CO2). Stable cell lines expressing the two eSAC components were generated by integrating
514 a bi-cistronic eSAC plasmid at engineered *lox* sites in the HeLa genome according to the protocol
515 described in (Khandelia et al., 2011). Upon transfection, DMEM media supplemented with 1 µg/ml
516 Puromycin was used to select transformed cells, and all the colonies were pooled to culture the
517 transformed cells used in the experiments.
518 To conduct dose-response analysis, each eSAC cell line was plated ~ 40-48 hours prior to the
519 start of the experiment in DMEM media without Puromycin. Doxycycline was added at the time of
520 plating to induce the expression of Frb-mCherry-Mps1. Prior to imaging, the cells were washed

521 with PBS. Fluorobrite media with 10% FBS, 1% Pen/Strep with or without Rapamycin were added
522 to each well.
523
524 **Genome editing HeLa cells using CRISPR/Cas9**
525 The guide RNAs (gRNAs) for in situ BUBR1 and BUB1 N-terminal mNeonGreen-tagging were 5'-
526 CAGGAUGGCGGCGGUGAAGA-3' and 5'-GGUUCAGGUUUGGCCGCUGC-3', respectively.
527 The gRNA for in situ MAD1 C-terminal mNeonGreen-tagging was 5'-
528 CAGACCGUGGCGUAGCCUGC-3'. Single guide RNAs (sgRNAs) were synthesized using the
529 EnGen sgRNA Synthesis Kit (for the *Streptococcus pyogenes*-originated Cas9, New England
530 Biolabs). The SpCas9-sgRNA ribonucleoprotein (RNP) complex was assembled at room
531 temperature in a buffer consisting of 20 mM of HEPES-KOH (pH 7.5), 150 mM of KCl, 1 mM of
532 $MgCl_2$, ten percent (by volume) of glycerol, and 1 mM of DTT using 100 pmol of SpCas9- 2×NLS
533 (the QB3 MacroLab) and 120 pmol of sgRNA. The RNP complex and 1.5 µg of a linearized
534 homology-directed repair template plasmid were transfected into 2×10^5 – 5×10^5 nocodazole-
535 arrested mitotic HeLa A12 cells using a Nucleofector and the associated Cell Line Kit R (Lonza)
536 following manufacturer's instructions. After five weeks, green fluorescence-positive mitotic cells
537 (arrested by 330 nM of nocodazole for 16 hours) were sorted directly into 96-well plates at 1
538 cell/well. Healthy colonies were subject to further validation by genotyping and sequencing, as
539 well as immunoblotting.
540 For genotyping, HeLa-A12 genomic DNAs were purified using the Wizard SV Genomic DNA
541 Purification System (Promega). Genotyping primers (BUBR1 forward primer 5'-
542 CCTGGTCACATCTGAGCTAT-3', BUBR1 reverse primer 5'-CTCAGTGAGACTCCAGTGTT-3',
543 BUB1 forward primer 5'-CCCTCTACATGAAGGCGCTA-3', BUB1 reverse primer 5'-
544 GCTCGCCCAAGGTAAACATT-3', MAD1 forward primer 5'-GGACTTTTCAGGGACGTGGT-3',
545 and MAD1 reverse primer 5'-GAGTTGGGAGGAGGGGACTC-3') were designed to bind outside
546 of homology arms to avoid false-positive colonies from integration of the homology-directed repair
547 template plasmid to an off-target genomic locus.
548
549 **Drug and RNAi treatments**
550 To induce the expression of the mCherry-Frb-Mps1 kinase domain doxycycline was added to a
551 final concentration of 2 ug/ml (stock concentration 2 mg/ml in DMSO) ~ 48 hours prior to the start
552 of the experiment. Prior to prior to the start of each experiment, Rapamycin was added ~ 1 hour
553 of the experiment to a final concentration of 500 nM (stock concentration 500 µM in DMSO) to
554 induce the dimerization of the eSAC kinase domain with the eSAC phosphodomain. Nocodazole

555 was added to the final concentration of 330 nM (stock concentration 330 μM in DMSO). The
556 cocktail of siRNA against five different B56 isoforms was added to a final concentration of 40 nM
557 (stock concentration 10 μM). The siRNA sequences were obtained from ref. (Nijenhuis et al.,
558 2014). Cell cycle synchronization was in G1/S was achieved by treating cells with 2.5 mM
559 thymidine (from a 100 mM stock in PBS) for 16-18 hours. Cells were washed with DMEM for
560 release from the G1/S arrest.
561
562 **Immunoprecipitation**
563 HeLa A12 cells constitutively expressing either MELT1-KI or MELT1-KI-M3 were
564 synchronized at G1/S by 2.5 mM of thymidine. 9 hours after being released from the
565 (double) thymidine block, cells were synchronized in metaphase using 10 μM MG132.
566 After another 1.5 hours, cells were scraped off the plate, washed once with PBS, pelleted,
567 snap-frozen, and stored at −80 °C. Cells were thawed, resuspended in the complete lysis
568 buffer (75 mM HEPES-HCl (pH 7.5), 150 mM KCl, 1.5 mM EGTA, 1.5 mM MgCl2, 10%
569 (by volume) glycerol, and 0.075% (by volume) Nonidet P-40 (AmericanBio); immediately
570 before use one cOmplete protease inhibitor cocktail tablet (EDTA-free, Roche
571 Diagnostics) and a phosphatase inhibitor cocktail (1 mM Na4P2O7, 0.1 mM Na3VO4, 5
572 mM NaF, and 2 mM sodium β-glycerophosphate) were added), and lysed for 1 hour at 4
573 °C while rotating. Cell lysates were then centrifuged at 18,000 g for 25 min at 4 °C. The
574 supernatant was subsequently cleared by control agarose beads for 1.5 hours at 4 °C to
575 reduce non-specific binding. Cleared supernatant was then mixed with mNeonGreen-
576 Trap agarose beads (ChromoTek) and rotated for 1.5 hours at 4 °C. Beads were washed
577 4 times using the lysis buffer. Finally, 2×Laemmli buffer (Bio-Rad Laboratories)
578 supplemented with β-mercaptoethanol was added to the beads. Samples were boiled in
579 a water bath for 10 min before subjecting to SDS-PAGE.
580 The following antibodies and working dilutions were used in immunoblotting:
581 SB1.3 antibody against BUB1 (Taylor et al., 2001), 1:500 or 1:1000, sheep polyclonal;
582 BUB3 antibody (Sigma B7811), 1:500, rabbit polyclonal; FKBP12 antibody (Abcam
583 ab2918), 1:2000, rabbit polyclonal; BUBR1 antibody (Bethyl A300-995A), 1:1000, rabbit
584 polyclonal.
585
586

587 **Long term live-cell imaging of HeLa cells**

588 Imaging was conducted over a period of 24 hours as described in detail previously (Chen et al.,
589 2019). We used either the Incucyte Zoom live cell imaging system (Sartorus Inc.) or the
590 ImageXpress Nano live cell imaging system (Molecular Devices Inc), both equipped with a 20x
591 Phase objective. To image cells on the Incucyte system, cells were plated in 12-well plastic tissue
592 culture plates, whereas they were plated in 24-well plate glass-bottom dishes (Corning) for the
593 ImageExpress Nano system. At each position, one phase, GFP, and mCherry image was
594 acquired every 10 minutes. The exposure times for mCherry and GFP images were adjusted to
595 minimize photobleaching while enabling accurate determination of intensity values. It should be
596 noted that the excitation sources, optics, and detector on the ImageXpress Nano and the Incucyte
597 microscope are entirely different. Therefore, the mCherry intensity values across different
598 experiments are not directly comparable.

599

600 **Image analysis**

601 Prior to intensity quantification, acquired images were pre-processed using functions from the
602 'Image Processing Toolbox' provided with Matlab as follows. First, the phase image sequence
603 was registered to remove any movement of the field of view between adjacent time point, and at
604 each time point, the same transform was applied to the GFP and mCherry images to register
605 them. Additionally, image intensity from a blank, unseeded well was used to for background
606 correction of the fluorescence channels. Next, GFP and mCherry fluorescence signals were
607 quantified using a custom graphical user interface (GUI) written in Matlab as described previously.
608 Briefly, this interface uses cross-correlation of each phase image with a circular kernel to identify
609 cells with circular shapes close to the diameter of the circular kernel. The centroids of these
610 shapes were then linked along the time axis. These images were presented to the user via the
611 GUI to: (a) discard false positive, non-mitotic cells or debris and (b) to visually correct the time of
612 entry into or exit from mitosis. The GUI then calculated the GFP and mCherry signals per cell as
613 the average fluorescence intensity

614 In all the dose-response assays discussed in this study, the phosphodomain is highly, and
615 constitutively, expressed in all cells, whereas the kinase domain is expressed conditionally by an
616 inducible promoter. Consequently, the amount of the kinase domain expressed varies from cell
617 to cell, and it is lower than the amount of the phosphodomain in most cells. Because of this design
618 of the eSAC system, the dosage of the dimerized signaling complex in a cell can be inferred from
619 the amount of Frb-mCherry-Mps1$^{500-817}$ in that cell. Therefore, we defined the dosage of the eSAC
620 signaling complex by quantifying the average mCherry fluorescence within a cell, and the

621 response as the duration of mitosis (the amount of time that the cell spends with a spherical
622 morphology that is characteristic of mitotic HeLa cells).

623

624 **Mathematical modeling**

625 **Modeling of dose-response curve for eSAC systems with Bub1 phosphodomains**

626 We constructed this model to understand the mechanisms underlying delayed mitotic exit
627 produced by the eSAC consisting of Bub1$^{221\text{-}620}$ and Bub1$^{441\text{-}620}$. In the equations below, we refer
628 to these phosphodomains simply as 'Bub1'. The eSAC activator complex is formed by the
629 dimerization of Bub1 with the kinase domain of Mps1. Upon phosphorylation by Mps1, Bub1 can
630 bind Mad1/2. The concentrations of different species of the Bub1 phosphodomain are related by
631 the equation:

632 $$[\text{Bub1}]_{\text{T}} = [\text{Bub1-Mps1-Mad1/2}] + [\text{Bub1-Mps1}] + [\text{Bub1}]. \quad (1)$$

633 Assuming reversible binding between phosphorylated Bub1 phosphodomain and Mad1/2
634 complex, we determined the concentration of eSAC activator complex, [Bub1-Mps1-Mad1/2] - it
635 saturates due to the finite concentration of Mad1-Mad2 complex (set at 100 nM, (Fig. S1A). Note,
636 that the phosphodomain can produce MCC only if it recruits Mad1/2. Bub1-Mps1 and Bub1 can
637 both bind BubR1 and Cdc20, but they do not participate in SAC signaling.

638 We modified a model of metaphase-to-anaphase transition by He et al. (He et al., 2011) as shown
639 in Figure S1B to capture key proteins and steps in the process of Bub1-mediated MCC formation
640 and to simulate the effect of MCC on mitotic exit. In the He model, Cyclin B ('CycB') is synthesized
641 at a constant rate and degraded by APC-Cdc20-dependent ubiquitination (denoted simply as
642 Cdc20). The abundance of CycB determines the activity of CDK1-CycB complexes. The activity
643 of the eSAC complex depends positively on CDK1-CycB activity and negatively on PP2-B55, a
644 counter-acting protein phosphatase (CAPP) (Bouchoux and Uhlmann, 2011; Sullivan et al.,
645 2004). This is a reasonable assumption, because recent data reveals that Bub1 must be
646 phosphorylated by both CDK1-CycB and Mps1 before it can bind Mad1 (Ji et al., 2017). The MCC
647 undergoes spontaneous dissociation, releasing BubR1, Cdc20 and inactive/open Mad2.
648 Furthermore, active APC-Cdc20 promotes the inactivation of closed/active Mad2 in MCC; this
649 positive feedback of active Cdc20 on its own release from the MCC accelerates the activation of
650 APC-Cdc20 during the transition into anaphase (Chen et al., 2019; He et al., 2011).

651 The molecular species, chemical reactions, parameters and constraints involved in the model are
652 presented in an Excel file and Table S1 (Supporting Information). A MATLAB script was used to

653 read this file and produce a file with Ordinary Differential Equations (ODEs) describing the rate of
654 change of all molecular species. We numerically integrated the ODEs to calculate the time
655 evolution of [CycB] and the other molecular species. For the initial conditions of species involving
656 BubR1 and Cdc20 bound to Bub1 phosphodomain (both signaling and non-signaling) we used
657 the equilibrium concentrations. These concentrations depended on the concentration of eSAC
658 activator complex and were calculated at the start of each simulation. The initial concentrations
659 of the following species were kept constant: [CycB] = 45 nM, [Mad2-Cdc20] = 0 nM, [MCC] = 25
660 nM, [CAPP] = 5 nM. In our model the system temporally evolves towards a steady state
661 corresponding to anaphase (low [CycB] and high [Cdc20]). We assume that a cell exits mitosis
662 when [CycB] drops below 1 nM (Fig. S1E). The choice of initial conditions does not qualitatively
663 affect the outcome of the model. Furthermore, the main result of this analysis – Bub1-BubR1
664 produces MCC at a higher rate than Bub1 – is robust, even though many different combinations
665 of parameters produce similar looking dose-response curves. Experimental measurements of
666 some of these parameters will be needed to constrain the model further.
667
668 **Modeling of dose-response curve for eSAC with MELT and KI motifs**
669 We constructed this model to simulate the observed dose-response data for the different eSAC
670 systems involving MELT and KI motifs. In these simulations, the phosphodomain consists of four
671 MELT motifs and either active or inactive KI motifs. All four MELT motifs in contact with the Mps1
672 kinase domain are assumed to be phosphorylated, whereupon they can recruit Bub1
673 (representing Bub1-Bub3 in this model. Upon binding to the MELT motif, Bub1 recruits BubR1
674 (representing BubR1-Bub3). The KI1 motif can bind to Bub1, whereas the KI2 motif can bind to
675 either Bub1 or BubR1 with characteristic binding affinities. The KI-bound Bub1 and BubR1 do not
676 participate in SAC signaling. Therefore, the KI motifs act like sinks that reduce Bub1 and BubR1
677 concentration. Interaction of the MELT motifs with Bub1 and BubR1 produces two types of
678 signaling complexes: MELpT-Bub1 or MELpT-Bub1-BubR1. For simplicity, we did not explicitly
679 model in detail how these signaling complexes catalyze MCC formation. Instead, we assume that
680 the MELpT-Bub1 and MELpT-Bub1-BubR1 complexes catalyze the assembly of MCC at the
681 apparent rates constants k_{MCC} and k'_{MCC}. A schematic diagram of the molecular mechanism
682 underlying this model is displayed in Figure S3A. The model simulates dose-response data in two
683 stages.
684
685 1. eSAC signaling cascade. We first calculate the steady-state concentrations of SAC signaling
686 proteins (Bub1 and BubR1) bound to the phosphorylated MELT motifs and KI motifs of an

eSAC phosphodomain. Using the steady-state concentrations of MELpT-Bub1 and MELpT-Bub1-BubR1, we calculate the rates of generation of MCC by the two phosphodomains, assuming that these rates is proportional their steady-state concentrations.

2. Mitotic delay. In the second stage of the model, we simulate the duration of mitosis, according to the overall reaction scheme developed by He et al. and discussed in the previous section.

Stage 1: Simulation of SAC protein recruitment by the eSAC phosphodomains

We assume that MELT and KI motifs in the eSAC phosphodomain interact with SAC proteins independently. We assigned the same rate of binding of the 'Bub1' protein to each MELT motif (*kf* in Table S2), but assigned a low unbinding rate (*kr*, Table S2) for the strong MELT motifs (MELT 1, 12 and 14), and a higher unbinding rate for the weak MELT motif (MELT 13) following previous studies (Chen et al., 2019; Vleugel et al., 2015). We also chose the dissociation constant for KI1-Bub1 binding to be equal to the dissociation constant for the KI2-BubR1 binding.

Each phosphorylated MELT motif can be in one of three possible states: MELpT (unbound MELT), MELpT-Bub1 (MELT bound by Bub1), and MELpT-Bub1-BubR1 (MELT bound by Bub1 and BubR1). Since there are four MELT motifs in each eSAC activator complex, the number of possible states for the phosphomimic become 3^4 = 81. Similarly, each KI motif of the phosphodomain can be in two states: bound or unbound. The time evolution of concentrations of different Bub1 and BubR1 bound states of eSAC activator complex is given by:

$$\dot{\mathbf{X}} = \mathbf{AX} \tag{1}$$

where $\mathbf{X} = \{x_1, x_1, \dots, x_N\}$ is a vector of concentrations of the $N = 81$ different Bub1 and BubR1 binding states of the eSAC, and **A** is the rate matrix. The binding of Bub1 and BubR1 to KI motifs is described by the set of equations:

$$\dot{y}_1 = \mathrm{kfbub} \cdot [\mathrm{Bub1}]_\mathrm{f} \cdot y_0 - \mathrm{krbub} \cdot y_1 - \mathrm{kfbub} \cdot [\mathrm{Bub1}]_\mathrm{f} \cdot y_1 - \mathrm{kfbubr} \cdot [\mathrm{BubR1}]_\mathrm{f} \cdot y_1 + \mathrm{krbubr} \cdot y_4 + \mathrm{krbub}' \cdot y_5 \tag{2}$$

$$\dot{y}_2 = \mathrm{kfbub} \cdot [\mathrm{Bub1}]_\mathrm{f} \cdot y_0 - \mathrm{krbub}' \cdot y_2 - \mathrm{kfbub} \cdot [\mathrm{Bub1}]_\mathrm{f} \cdot y_2 + \mathrm{krbub}' \cdot y_5 \tag{3}$$

$$\dot{y}_3 = \mathrm{kfbubr} \cdot [\mathrm{BubR1}]_\mathrm{f} \cdot y_0 - \mathrm{krbubr} \cdot y_3 - \mathrm{kfbub} \cdot [\mathrm{Bub1}]_\mathrm{f} \cdot y_3 + \mathrm{krbubr} \cdot y_4 \tag{4}$$

$$\dot{y}_4 = \mathrm{kfbubr} \cdot [\mathrm{BubR1}]_\mathrm{f} \cdot y_1 - \mathrm{krbubr} \cdot y_3 - \mathrm{krbub} \cdot y_3 - \mathrm{krbubr} \cdot y_4 \tag{5}$$

$$\dot{y}_5 = \mathrm{kfbub}' \cdot [\mathrm{Bub1}]_\mathrm{f} \cdot y_1 + \mathrm{kfbub} \cdot [\mathrm{Bub1}]_\mathrm{f} \cdot y_2 - \mathrm{krbub} \cdot y_5 - \mathrm{krbub}' \cdot y_5, \tag{6}$$

where, y_0 is the concentration of free KI motifs (both KI motifs unbound),

$$y_1 = [\text{KI1-Bub1}],$$

$$y_2 = [\text{KI2-Bub1}],$$

$$y_3 = [\text{KI2-BubR1}],$$

$$y_4 = [\text{KI1-Bub1}, \text{KI2-BubR1}],$$

$$y_5 = [\text{KI1-Bub1}, \text{KI2-Bub1}].$$

$[\text{Bub1}]_\text{f}$ and $[\text{BubR1}]_\text{f}$ are the concentrations of free Bub1 and BubR1 in the cytoplasm, respectively. The parameters kfbub and kfbub' are the rate constants for Bub1 binding to the first and the second KI motif respectively (krbub and krbub' are the corresponding unbinding rates), and kfbubr and krbubr are the binding (unbinding) rates between BubR1 and KI2.

The concentrations satisfy the constraints:

$$[\text{eSAC}] = \sum_{i=1}^{N} x_i \tag{7}$$

$$[\text{Bub1}]_\text{T} = [\text{Bub1}]_\text{f} + y_1 + y_2 + y_4 + 2y_5 + \sum_{i=1}^{N} n_i \cdot x_i \tag{8}$$

$$[\text{BubR1}]_\text{T} = [\text{BubR1}]_\text{f} + y_3 + y_4 + \sum_{i=1}^{N} m_i \cdot x_i \tag{9}$$

Here, x_i is the concentration of the i-th species, n_i = number of Bub1 units bound to i-th species, and m_i = number of BubR1 units bound to the i-th species. We assume $[\text{Bub1}]_\text{T} = 100\ \text{nM}$ and $[\text{BubR1}]_\text{T} = 100\ \text{nM}$. The equilibrium concentration of each state was obtained by numerically solving $\dot{\mathbf{X}} = \dot{y}_i = 0, i = 1,2 \ldots,5$.

In experiments, the concentration of eSAC activator complex is measured in arbitrary units of mCherry fluorescence (a. u.), whereas in our model the unit of concentration is nano moles (nM). In our simulations, we chose the maximum value of concentration of eSAC activator complex (the value corresponding to 20 a. u. in experiments) to be 200 nM. For easier comparison to experimental figures, in our simulation results the eSAC activator complex concentration is expressed in arbitrary units, with 1 a. u. of fluorescence corresponding to 10 nM.

Figure S3A shows the abundance of different Bub1 and BubR1-bound states as functions of the total concentration of eSAC activator complex for KI1*-KI2*. At low eSAC concentrations, the eSAC tends to be highly loaded, with Bub1 and BubR1 on every MELT motif. However, for cells

with a high eSAC concentration, [eSAC] >> $[\text{Bub1}]_T$, the most abundant eSAC species is one that does not bind any Bub1 at all (not shown), followed by species that bind either Bub1 or Bub1-BubR1 at only one of the MELT motifs. We define the sum of concentration of MELpT-Bub1 and MELpT-Bub1-BubR1 as $[\text{eSAC}]_T$:

$$[\text{eSAC}]_\text{T} = [\text{MELpT-Bub1}] + [\text{MELpT-Bub1-BubR1}] \tag{10}$$

$$[\text{MELpT-Bub1}] = \sum_{i=1}^{N} (n_i - m_i) \cdot x_i \tag{11}$$

$$[\text{MELpT-Bub1-BubR1}] = \sum_{i=1}^{N} m_i \cdot x_i \tag{12}$$

Formation of MCC by the eSAC signaling complexes

We assume that the recruitment of SAC proteins (Bub1 and BubR1) to MELT motifs of the eSAC activator complexes enables the incorporation of Cd20 into MCC. Since different species catalyze this reaction at different rates, we define the effective rate of conversion, k_asmcc, as the concentration-weighted sum of the conversion rates of each eSAC complex:

$$k_\text{asmcc} = \frac{1}{[\text{eSAC}]_\text{T}} \cdot \left[k_\text{MCC} \cdot \sum_{i=1}^{N} (n_i - m_i) \cdot x_i \; + \; k'_\text{MCC} \cdot \sum_{i=1}^{N} m_i \cdot x_i \right], \tag{13}$$

where k_MCC and k'_MCC are the MCC formation rates due to MELpT-Bub1 and MELpT-Bub1-BubR1, respectively. Note, for most species, the rate of MCC generation is additive. For example, $k_{0012} = k_\text{MCC} + k'_\text{MCC}$ for a phosphodomain that binds only Bub1 at the 13th MELT motif and Bub1-BubR1 at 14th MELT motif (Table S3). Using $[\text{eSAC}]_\text{T}$ and k_asmcc as inputs for the He model (discussed below), we calculated the time evolution of Cyclin B concentration and from it the time in mitosis.

Stage 2: The effect of MCC produced on exit from mitosis

To calculate the effect of MCC generated by the eSAC on mitotic exit, we used a simplified version of the model of the mitotic checkpoint proposed by the He model (He et al., 2011). Active eSAC signaling complexes (eSAC_A) generate MCC, as described in the previous section. The temporal dynamics of our mitotic checkpoint model are determined by the ordinary differential equations:

$$\frac{\text{d}[\text{CycB}]}{\text{d}t} = k_\text{scyc} - \left(k_\text{dcyc} + k_\text{dcyc,c20} \cdot [\text{Cdc20}]\right) \cdot [\text{CycB}] \tag{14a}$$

$$\frac{\mathrm{d}[\mathrm{eSAC_A}]}{\mathrm{d}t} = k_{\mathrm{ancyc}} \cdot [\mathrm{CycB}] \cdot ([\mathrm{eSAC}]_\mathrm{T} - [\mathrm{eSAC_A}]) - k_{\mathrm{in,capp}} \cdot [\mathrm{CAPP}] \cdot [\mathrm{eSAC_A}] \qquad (14b)$$

$$\frac{\mathrm{d}[\mathrm{MCC}]}{\mathrm{d}t} = k_{\mathrm{asmcc}} \cdot [\mathrm{Cdc20}] \cdot [\mathrm{eSAC}]_\mathrm{A} - \left(k_{\mathrm{dimcc}} + k_{\mathrm{imad}} + k_{\mathrm{imad,c20}} \cdot [\mathrm{Cdc20}]\right) \cdot [\mathrm{MCC}] \qquad (14c)$$

$$\frac{\mathrm{d}[\mathrm{CAPP}]}{\mathrm{d}t} = k_{\mathrm{acapp}} \cdot ([\mathrm{CAPP}]_\mathrm{T} - [\mathrm{CAPP}]) - k_{\mathrm{icapp,cyc}} \cdot [\mathrm{CycB}] \cdot [\mathrm{CAPP}] \qquad (14\mathrm{d})$$

In these equations, $[\mathrm{CycB}] = [\mathrm{CDK\text{-}CycB}]$, $[\mathrm{Cdc20}] = [\mathrm{APC\text{-}Cdc20}]$, $[\mathrm{eSAC}]_\mathrm{T}$ is the total concentration of Bub1 and BubR1-bound eSAC signaling complexes (Eq. 10), which is either in the active, signaling-competent state $\mathrm{eSAC_A}$, or the inactive state, $[\mathrm{eSAC_I}] = [\mathrm{eSAC}]_\mathrm{T} - [\mathrm{eSAC_A}]$. [MCC] and [CAPP] refer to the concentrations of the mitotic checkpoint complex and the CDK-counteracting protein phosphatase, respectively. In addition, the total concentration of Cdc20 is:

$$[\mathrm{Cdc20}]_\mathrm{T} = [\mathrm{Cdc20}] + [\mathrm{MCC}]$$

Here, the subscript T indicates total concentration. The values of the parameters in the model and of the fixed concentrations of some components, as listed in Table S2, are taken from (He et al., 2011).

<u>Simulation of time in mitosis</u>

To simulate 'time in mitosis', we assume that a cell exits mitosis when [CycB] drops below 1 nM. We numerically integrated Ordinary Differential Equations (ODEs) to calculate the time evolution of [CycB] and the other components of the mitotic checkpoint. As before, the initial conditions for the simulation are chosen to be [CycB] = 45 nM, $[\mathrm{eSAC_A}] = 0$, [MCC] = 25 nM, and [CAPP] = 5 nM. The qualitative aspects of our results do not change if the initial conditions are changed a little bit. Figure S3C displays typical time courses for [CycB], for different eSACs, for [eSAC activator complex] = 10 a. u. The system always comes out of mitosis (as seen by the drop in [CycB]), albeit after different time delays.

Statistical analysis

To determine the overall trend in the dose-response data, the data were first binned (in MATLAB) and then the mean values of each bin were overlayed on the data. The number of observations, technical replicates are noted in the figure legends. These mean values were fit with a four-parameter sigmoidal curve using the GraphPad Prism 9 software. Statistical significance of the difference between the mean values in Figure 5B was assessed using the unpaired t-test with Welch's correction.

804 **Figure 1**

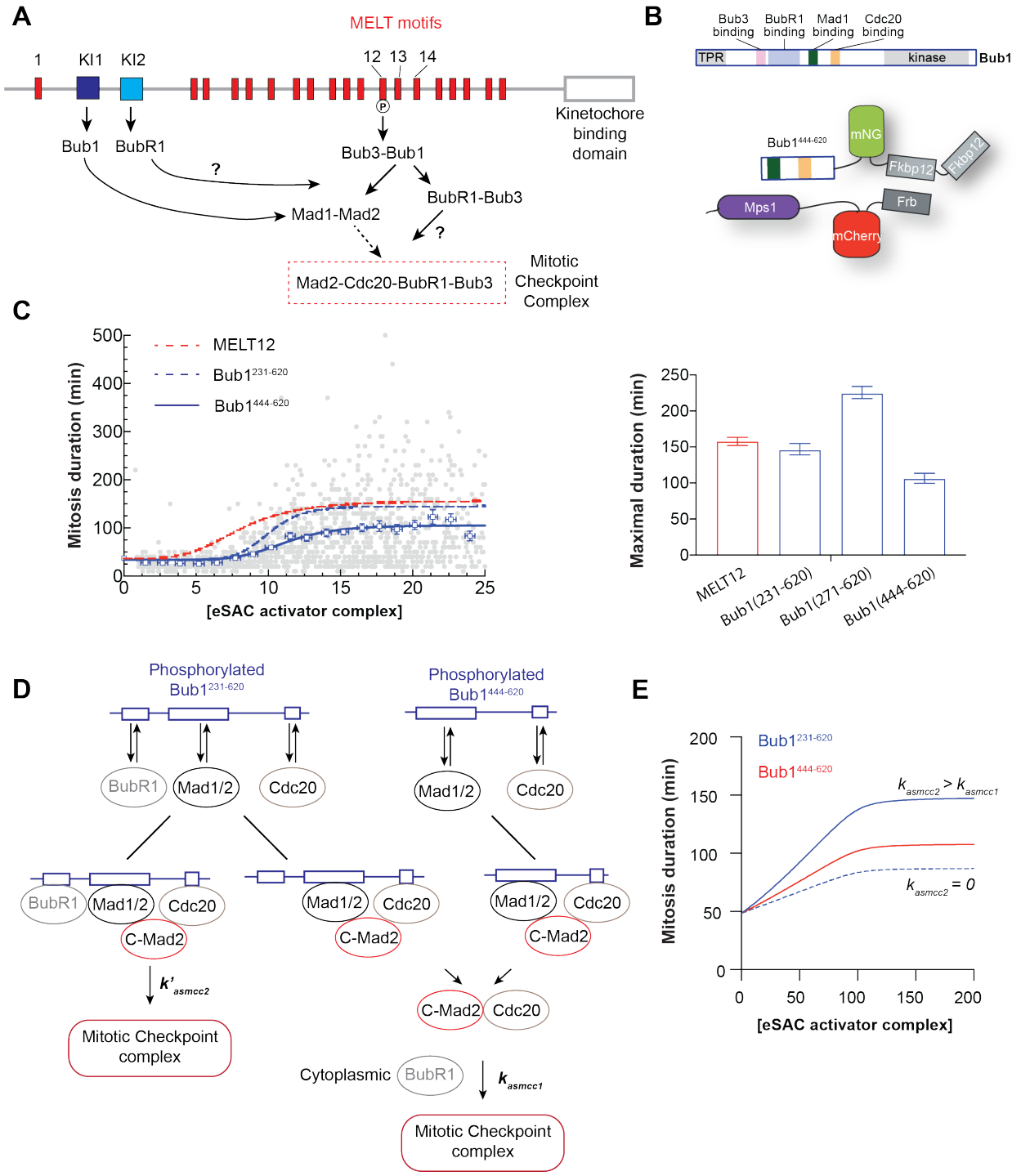

805

806 **Figure 1 The contribution of Bub1-BubR1 heterodimerization to MCC assembly during**
807 **eSAC signaling. A** Schematic at the top displays the domain organization of human Knl1. Below
808 is a simplified schematic displaying the pathways that recruit SAC signaling proteins to unattached
809 kinetochores. **B** Schematic at the top displays the domain organization of human Bub1. The

810 cartoon represents the ectopic SAC activation or 'eSAC' system. **C** Dose-response data for an
811 eSAC system that uses Bub1$^{444-620}$ as the phosphodomains. Each gray circle displays the average
812 cellular mCherry fluorescence (X axis) and the time in mitosis (Y axis) for a single cell (n = 1920
813 from 2 experiments; 139 and 155 are the lower and upper 95% confidence intervals). Blue
814 squares represent mean values of the dose-response data binned according to mCherry
815 fluorescence. Vertical and horizontal lines represent S.E.M. The solid blue curve displays the
816 least squares 4-parameter sigmoidal fit to the binned mean values. Sigmoidal fits for dose-
817 response data for one MELT motif (MELT12, dashed red curve) and an extended Bub1$^{231-620}$
818 phosphodomain containing the Bub3- and BubR1-binding sites (dashed blue curve) from our
819 previous study have been super-imposed for comparison (Chen et al., 2019). Bar graph on the
820 right displays the maximal mitotic duration estimated by the sigmoidal fit. Vertical lines represent
821 95% confidence interval on the fit parameter. **D** Cartoon displays the simplified scheme used to
822 simulate the generation of MCC by the eSAC system. **E** Numerical simulation of the dose-
823 response curves by assuming the assembly of signaling complexes and ultimately the MCC as
824 show in **D** followed by a bi-stable switch based on negative feedback described by He et al (He
825 et al., 2011).
826
827
828

829 **Figure 2**

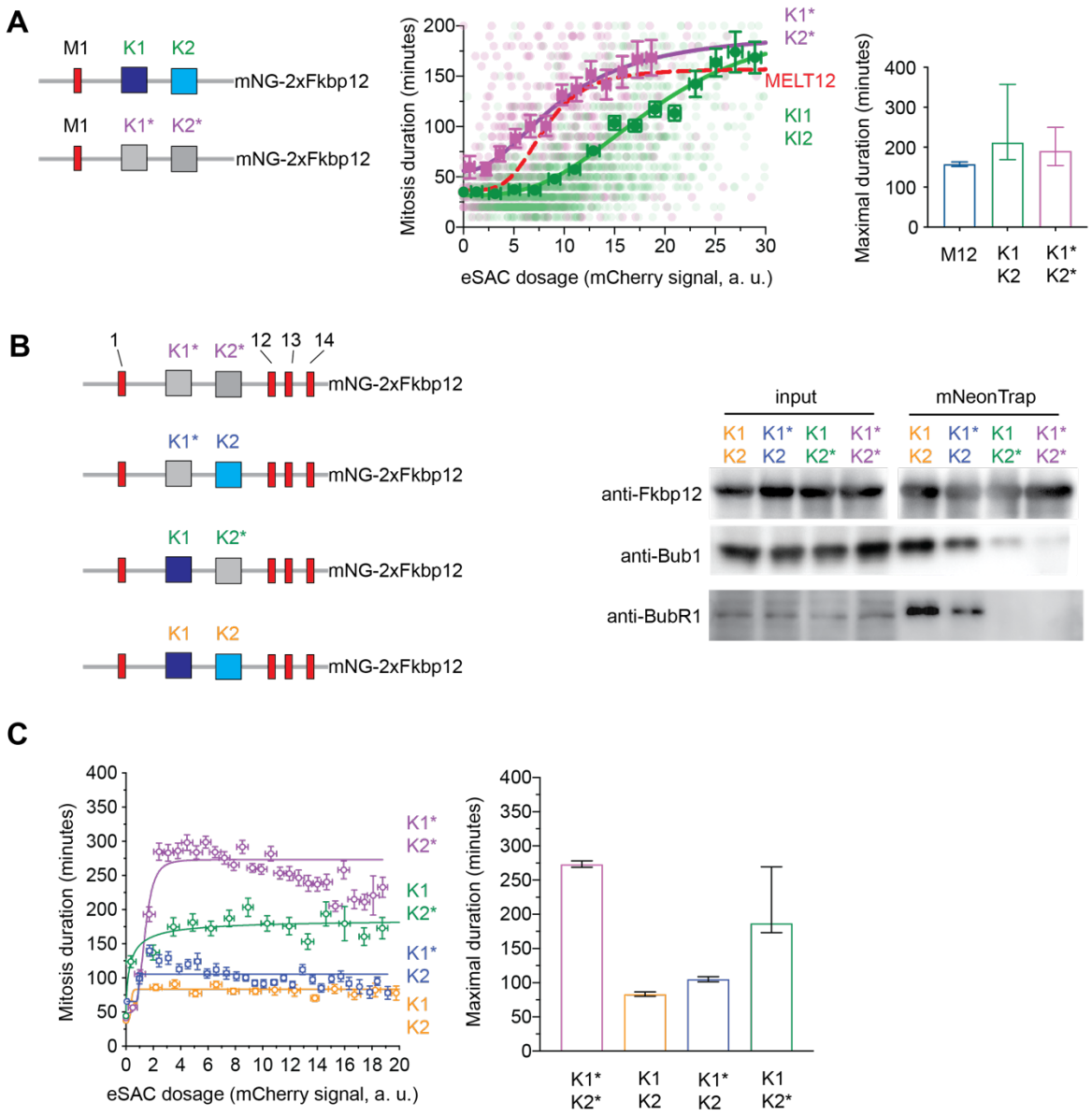

830

831 **Figure 2 Recruitment of Bub1 and BubR1 by the KI motifs in KNL1 and their contribution**
832 **to eSAC signaling. A** Left: Schematic of the two phosphodomains used to test whether the KI
833 motifs contribute to MCC assembly mediated by the MELT motif in the eSAC phosphodomain.
834 KI1-KI2 indicates phosphodomain with intact KI motifs, KI1*-KI2* indicates phosphodomains
835 wherein the KI motifs are inactivated using suitable point mutations (see Methods for details).
836 Scatter plot in the middle displays the dose-response data for the two phosphodomains (n = 1888
837 in green and n = 836 in magenta from ≥ 2 experiments respectively for KI1-KI2 and KI1*-KI2*;
838 symbol usage follows the scheme established in 1**C**). The bar graph on the right displays the

839 maximal mitotic duration predicted by 4-parameter sigmoidal fits to the binned mean values as in
840 Figure 1C. Vertical lines display 95% confidence intervals on the fit parameter. **B** Left: Schematic
841 of the phosphodomains consisting of 4 MELT motifs and either active or inactive (indicated by *)
842 KI motifs. Right: Immunoprecipitation of the eSAC phosphodomains using mNeonGreenTrap
843 beads followed by Western blot analysis to probe for the co-IP of the indicated proteins. **C** Dose-
844 response data for the indicated phosphodomains. Only the binned mean values are shown for
845 clarity. Statistical analysis performed as in 1D (n = 1019, 1024, 666, and 3219 for KI1-KI2, KI1-
846 KI2*, KI1*-K2, and KI1*-KI2* respectively from ≥ 2 experiments). Bar graph on the right displays
847 the maximal time in mitosis predicted by the sigmoidal fits.
848

849 **Figure 3**

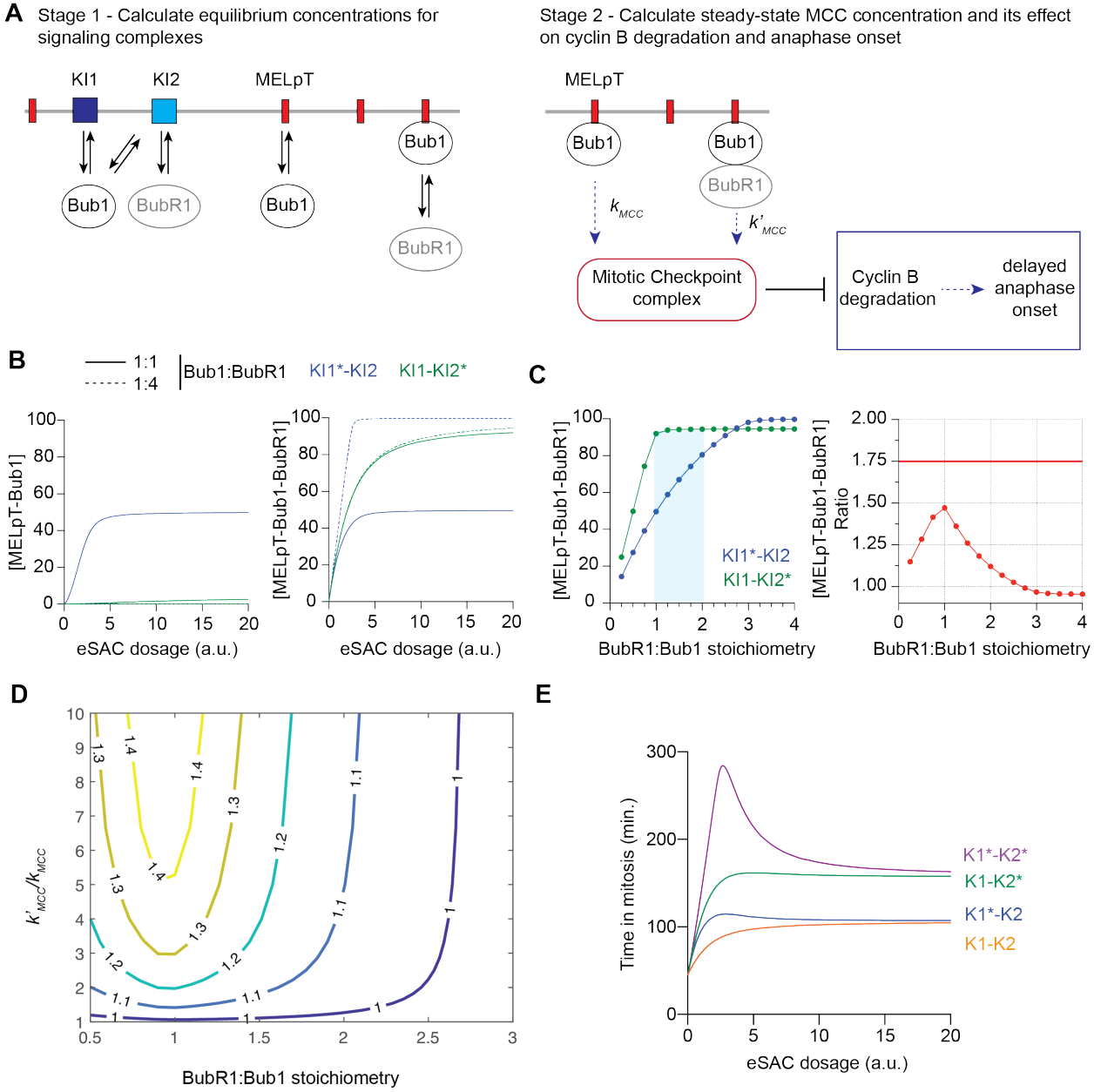

850

851 **Figure 3 Numerical simulation of the dose-response data for the eSAC phosphodomains**
852 **containing KI motifs. A** Schematic of the two-stage model used to simulate the dose-response
853 curves. **B** The influence of Bub1-BubR1 stoichiometry and the differential depletion of Bub1 and
854 BubR1 by the KI motifs in the simulations on the equilibrium concentrations of the two signaling
855 complexes formed on phosphorylated MELT motifs. **C** Comparison of the equilibrium
856 concentration of the MELpT-Bub1-BubR1 complex assembled by KI1*-KI2 and KI1-KI2* (left) and
857 their ratio (right) as a function of the Bub1-BubR1 stoichiometry. For the two phosphodomains to
858 generate different responses, the Bub1-BubR1 stoichiometry must be around 1:1 (indicated by

859 the blue shaded area). **D** Contour plot shows the ratio of the maximal responses produced by
860 KI1*-KI2 and KI1-KI2* as a function of the Bub1-BubR1 stoichiometry and the ratio of the rates at
861 which the MELpT-Bub1-BubR1 and the MELpT-Bub1 signaling complexes produce MCC (i.e.,
862 k'_{MCC}/k_{MCC}). **E** Simulation of the dose-response curves for the four phosphodomains using the
863 same set of parameter values.
864

865 **Figure 4**

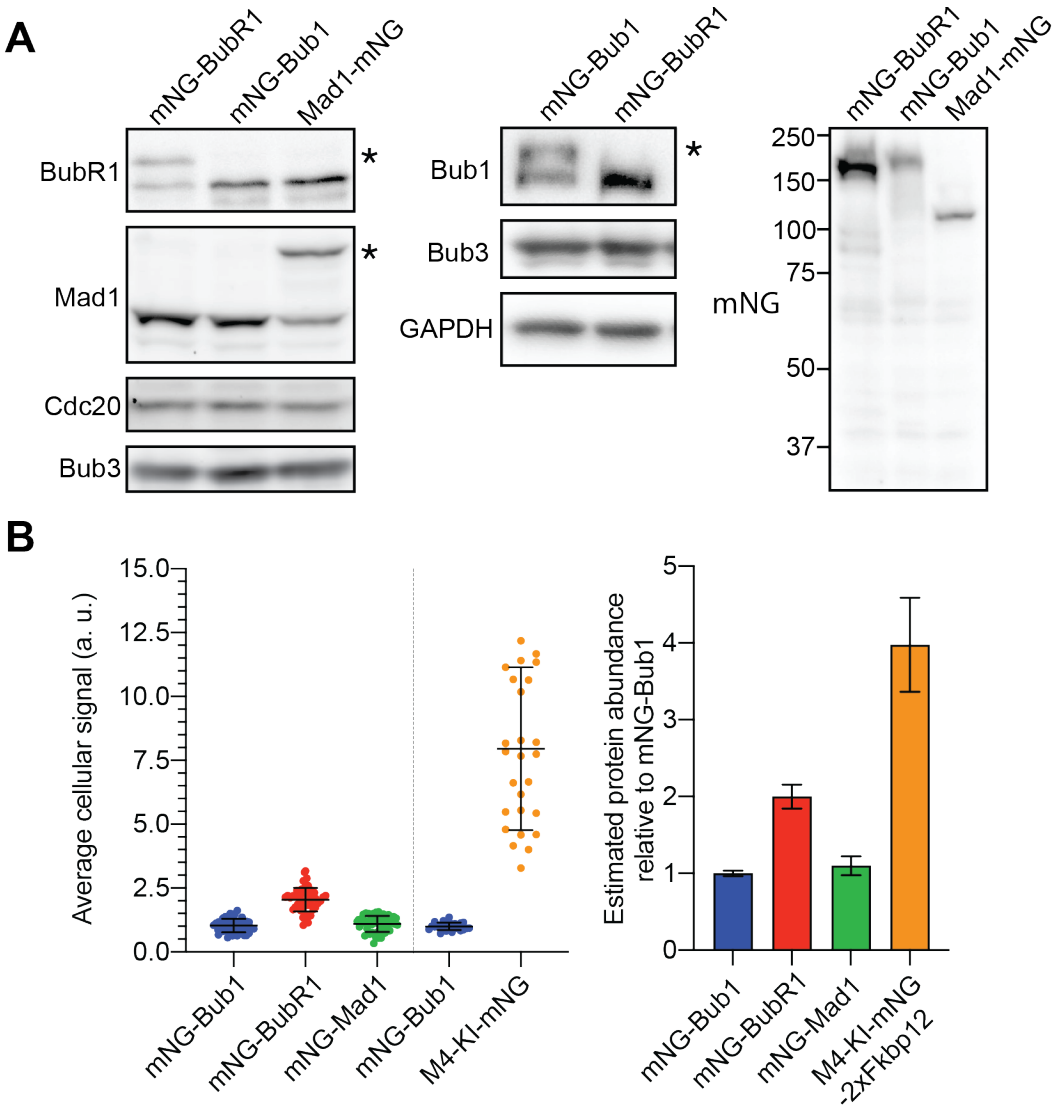

866

867 **Figure 4 Generation of CRISPR/Cas9 genome-edited HeLa cell lines expressing**
868 **mNeonGreen-Bub1, mNeonGreen-BubR1, and Mad1-mNeonGreen. A** Western blots show
869 that showing that roughly half the BubR1 and Mad1 (left) and Bub1 (middle) is tagged with
870 mNeonGreen in the three partially genome-edited cell lines (asterisks on the right of each
871 displayed blot mark the mNG fusion protein). Western blot on the right shows whole cell extracts
872 of the three cell lines probed with anti-mNeonGreen antibodies. **B** Average mNG-Bub1, mNG-
873 BubR1, Mad1-mNG, and M4-KI1-KI2-mNG-2xFkbp12 signals from mitotic HeLa cells (left) and
874 estimation of the relative protein abundance, assuming that the total protein is twice as high as
875 the abundance of the mNG-labeled species (mean ± std. dev.).

876

877 **Figure 5**

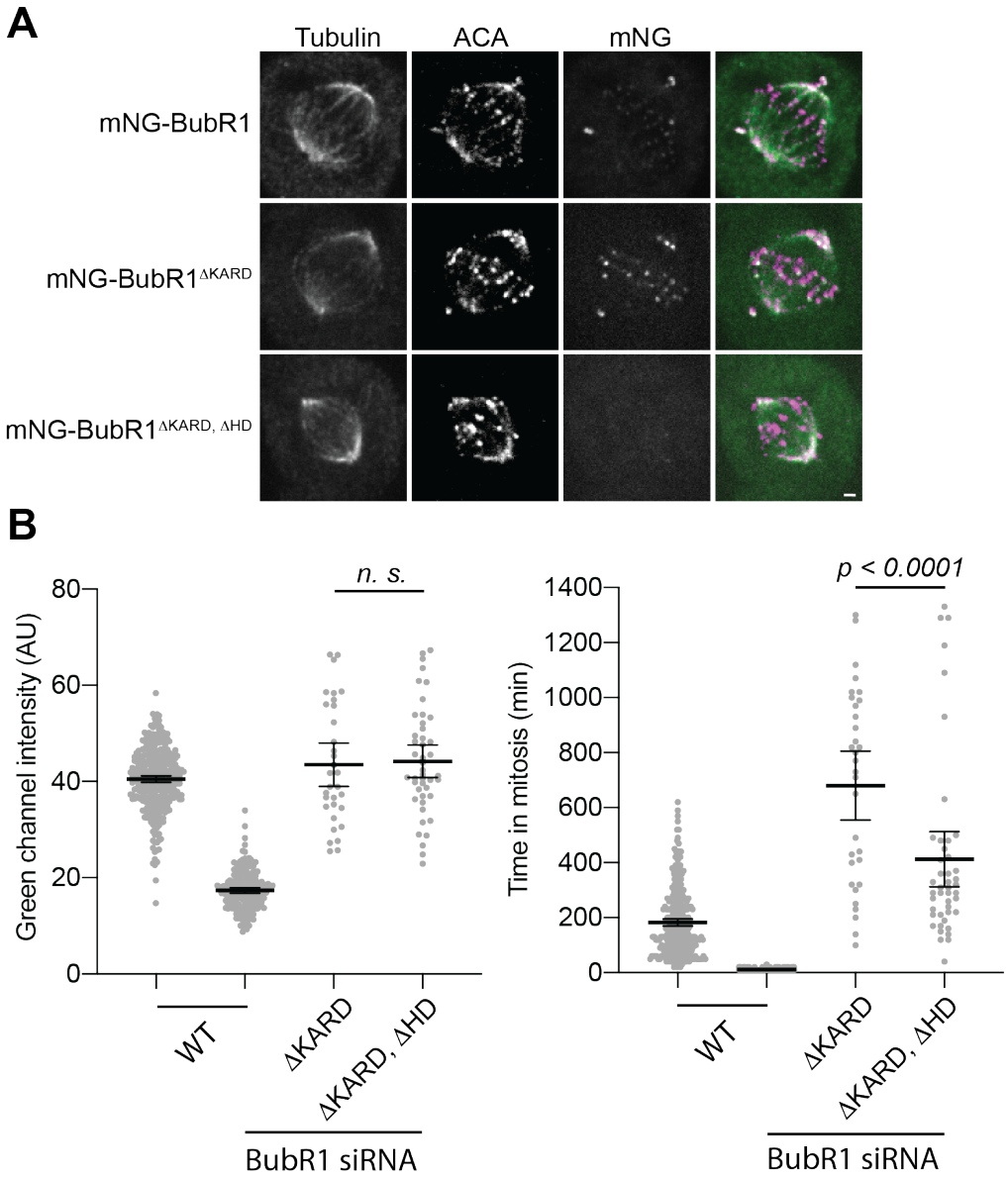

878

879 **Figure 5 Recruitment of BubR1 by BuB1 per se contributes to the signaling strength of the**
880 **SAC. A** Micrographs of representative cells displaying the indicated antigens at the top. The top
881 row displays micrographs of the partially genome-edited cell line expressing mNG-BubR1. The
882 bottom two rows display representative cells after endogenous BubR1 was knocked down and
883 the indicated mutant, mNG-tagged version was ectopically expressed (scale bar ~ 1.22 microns).
884 **B** Scatterplot on the left displays the duration of mitosis of either genome-edited cells expressing
885 WT BubR1 or cells that ectopically expressed the indicated mutant after BubR1 RNAi in media
886 containing 50 nM nocodazole. Scatterplot on the right displays the average intracellular
887 mNeonGreen signal from the same cells (mean ± 95% confidence intervals).

888 **Supplementary Figure 1**

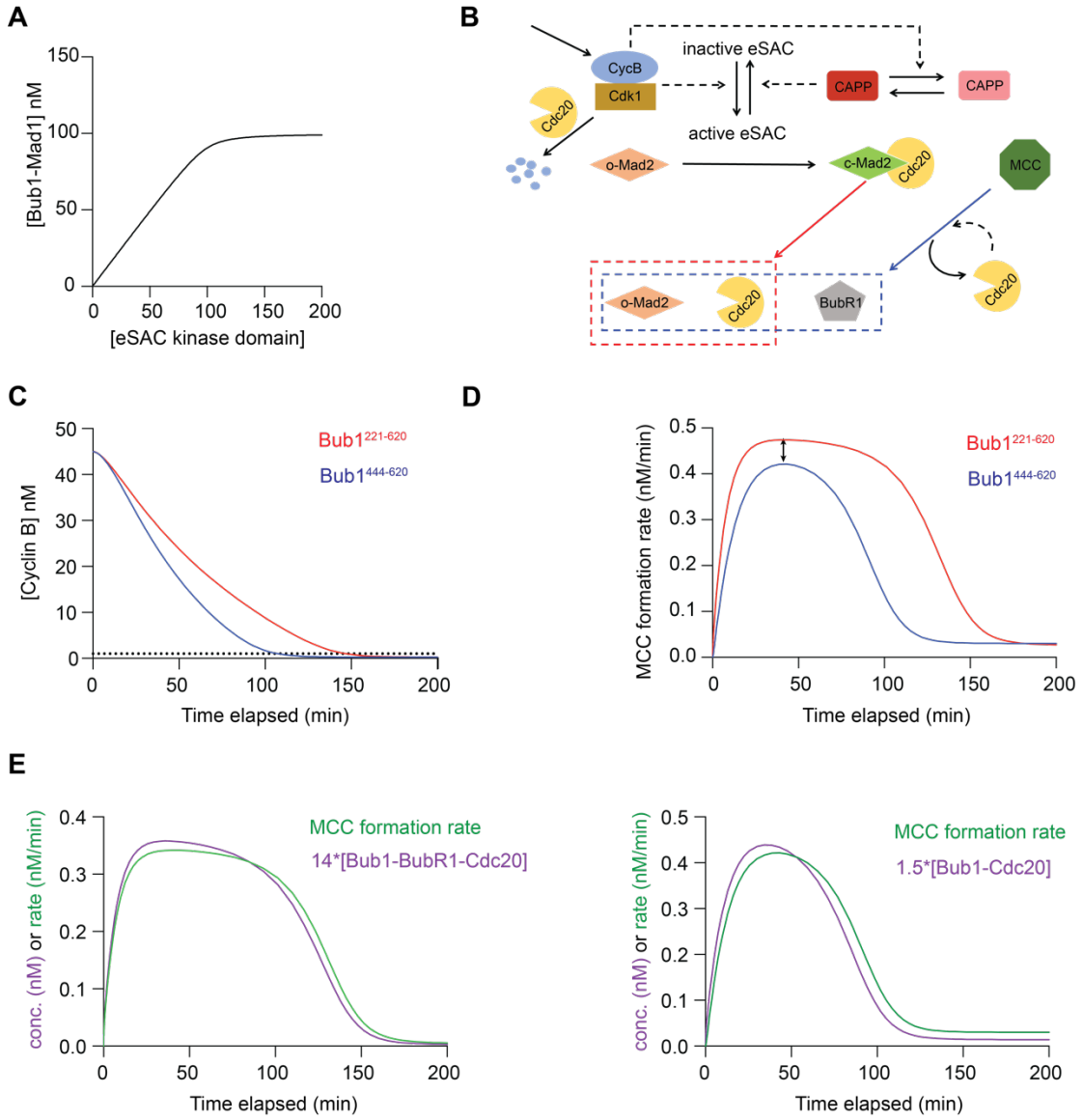

889
890
891 **Figure S1 Simulation of the dose-response curves for the Bub1 eSAC system. A** The
892 amount of the eSAC signaling complex (Bub1-Mad1) saturates due to the limited availability of
893 Mad1 (100 nM). **B** Schematic of the model used to simulate the dose-response data for the "full"
894 and "truncated" Bub1 phosphodomain used in the eSAC system. **C** Temporal evolution of Cyclin
895 B concentration for the two eSAC systems. **D** Assessment of MCC formation rates for the full and
896 truncated phosphodomain. **E** Superimposition of the dynamics of the MCC formation rate and the
897 concentration of signaling complexes that produce MCC.
898
899

900 **Supplementary Figure 2**

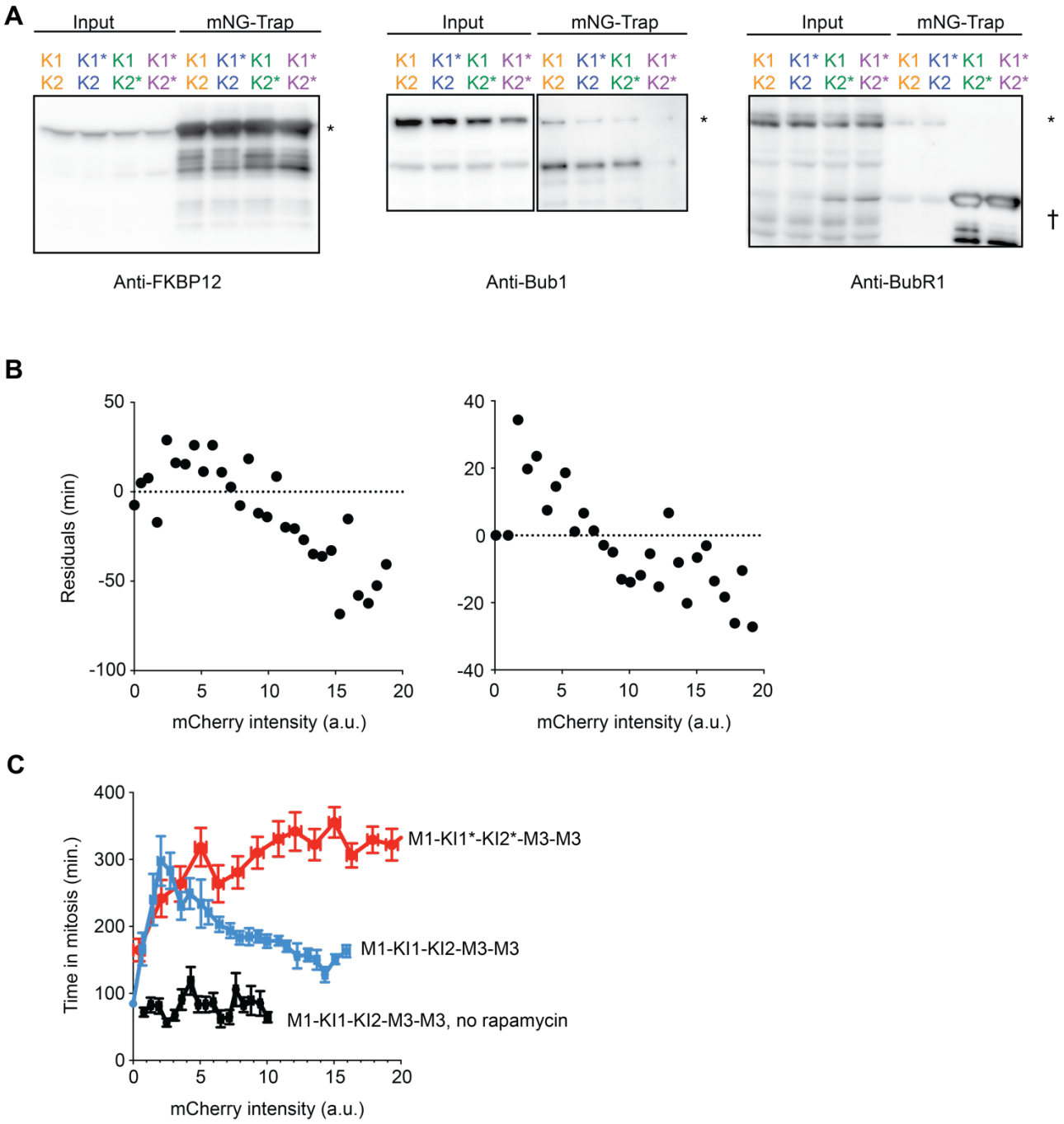

901
902
903
904 **Supplementary Figure 2 A** Western blot probing for the indicated protein for assessing the co-
905 immunoprecipitation of Bub1 and BubR1 with the indicated eSAC phosphodomain (at the top).
906 The asterisk marks the position of the band corresponding to the full-length protein. The cross
907 marks bands that likely degradation products of the full-length protein. **B** Residual plots from a 4-

908 parameter sigmoidal fit to the dose-response data for the KI1*-KI2* (left) and KI1-KI2* (right)
909 phosphodomains. **C** Dose-response data for the indicated phosphodomains. Circles represent
910 average values of binned data (vertical and horizontal lines display standard error on each mean
911 value. n= 498, 1313, and 394 respectively for M1-KI1-KI2-M3-M3, M1-KI1*-KI2*-M3-M3, and M1-
912 KI1-KI2-M3-M3 without rapamycin respectively pooled from two or more experiments).
913

914 **Supplementary Figure 3**
915

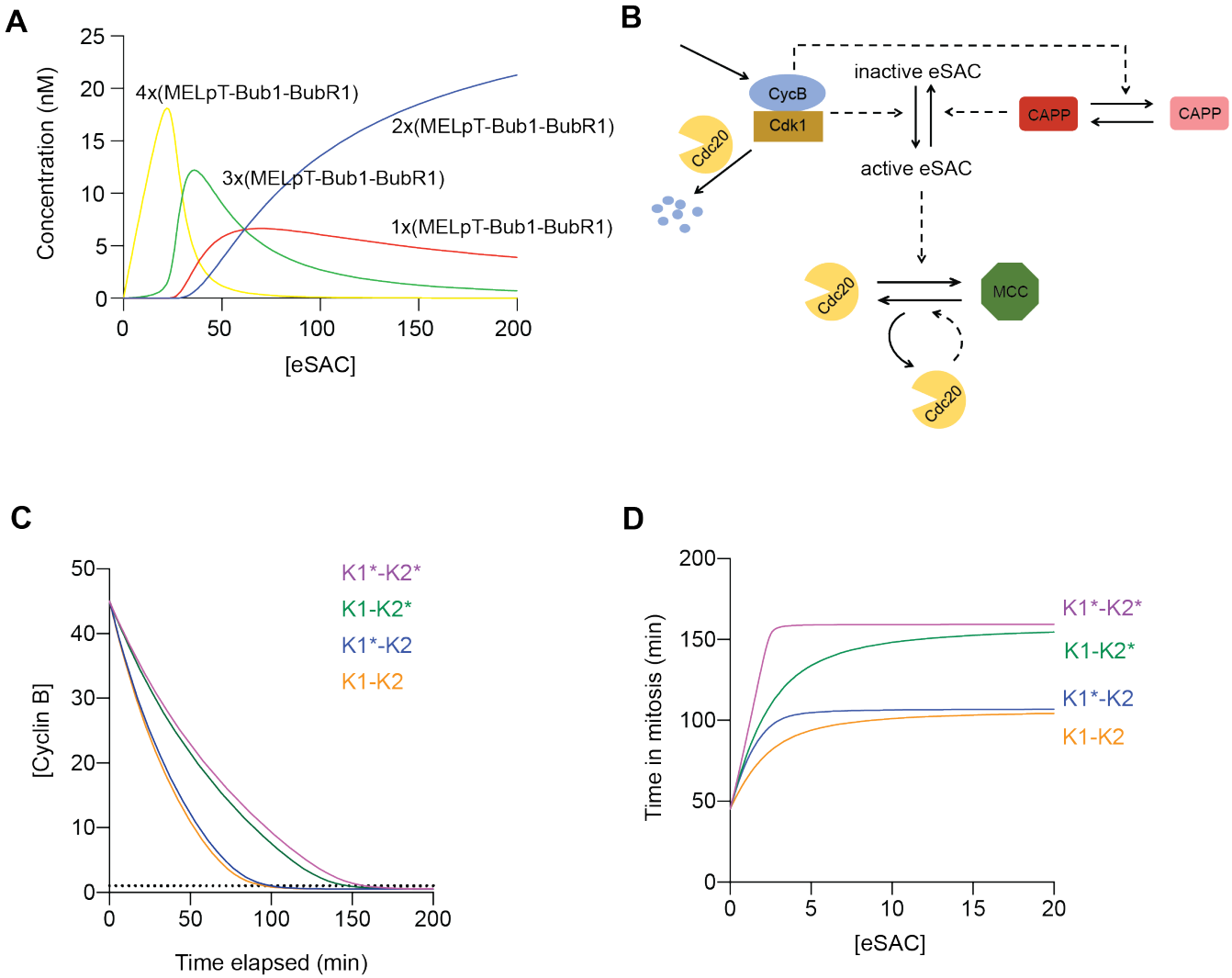

916
917
918 **Figure S3 Simulation of the dose-response data for eSAC systems containing the KI motifs**
919 **and MELT motifs. A** Abundance of the indicated eSAC signaling complex (of the form n*(MELpT-
920 Bub1-BubR1)) as a function of the total concentration of the eSAC activator complex. The number
921 n indicates the number of MELT motifs bound to Bub1-BubR1. Also see Table S3. **B.** Schematic
922 of the model used to simulate the dose-response data for eSAC with MELT and KI motifs. **C**
923 Temporal evolution of Cyclin B concentration for the MELT and KI motif eSAC system. **D**
924 Simulation of dose-response curves for the four phosphodomains without synergistic interactions
925 between the MELT motifs.
926

927 **References**

928 Bolanos-Garcia, V.M., Lischetti, T., Matak-Vinkovic, D., Cota, E., Simpson, P.J., Chirgadze, D.Y.,
929 Spring, D.R., Robinson, C.V., Nilsson, J., and Blundell, T.L. (2011a). Structure of a Blinkin-BUBR1
930 complex reveals an interaction crucial for kinetochore-mitotic checkpoint regulation via an
931 unanticipated binding Site. Structure *19*, 1691-1700.
932 Bolanos-Garcia, Victor M., Lischetti, T., Matak-Vinković, D., Cota, E., Simpson, Pete J., Chirgadze,
933 Dimitri Y., Spring, David R., Robinson, Carol V., Nilsson, J., and Blundell, Tom L. (2011b). Structure
934 of a Blinkin-BUBR1 Complex Reveals an Interaction Crucial for Kinetochore-Mitotic Checkpoint
935 Regulation via an Unanticipated Binding Site. Structure *19*, 1691-1700.
936 Bouchoux, C., and Uhlmann, F. (2011). A quantitative model for ordered Cdk substrate
937 dephosphorylation during mitotic exit. Cell *147*, 803-814.
938 Chen, C., Whitney, I.P., Banerjee, A., Sacristan, C., Sekhri, P., Kern, D.M., Fontan, A., Kops, G.,
939 Tyson, J.J., Cheeseman, I.M.*, et al.* (2019). Ectopic Activation of the Spindle Assembly Checkpoint
940 Signaling Cascade Reveals Its Biochemical Design. Curr Biol *29*, 104-119 e110.
941 Collin, P., Nashchekina, O., Walker, R., and Pines, J. (2013). The spindle assembly checkpoint
942 works like a rheostat rather than a toggle switch. Nat Cell Biol *15*, 1378-1385.
943 Dick, A.E., and Gerlich, D.W. (2013). Kinetic framework of spindle assembly checkpoint signalling.
944 Nat Cell Biol *15*, 1370-1377.
945 Faesen, A.C., Thanasoula, M., Maffini, S., Breit, C., Muller, F., van Gerwen, S., Bange, T., and
946 Musacchio, A. (2017). Basis of catalytic assembly of the mitotic checkpoint complex. Nature.
947 Foley, E.A., Maldonado, M., and Kapoor, T.M. (2011). Formation of stable attachments between
948 kinetochores and microtubules depends on the B56-PP2A phosphatase. Nat Cell Biol *13*, 1265-
949 1271.
950 He, E., Kapuy, O., Oliveira, R.A., Uhlmann, F., Tyson, J.J., and Novák, B. (2011). System-level
951 feedbacks make the anaphase switch irreversible. Proceedings of the National Academy of
952 Sciences.
953 Ji, Z., Gao, H., Jia, L., Li, B., and Yu, H. (2017). A sequential multi-target Mps1 phosphorylation
954 cascade promotes spindle checkpoint signaling. Elife *6*.
955 Jia, L., Li, B., and Yu, H. (2016). The Bub1-Plk1 kinase complex promotes spindle checkpoint
956 signalling through Cdc20 phosphorylation. Nat Commun *7*, 10818.
957 Khandelia, P., Yap, K., and Makeyev, E.V. (2011). Streamlined platform for short hairpin RNA
958 interference and transgenesis in cultured mammalian cells. Proc Natl Acad Sci USA *108*, 12799-
959 12804.
960 Kiyomitsu, T., Murakami, H., and Yanagida, M. (2011). Protein interaction domain mapping of
961 human kinetochore protein Blinkin reveals a consensus motif for binding of spindle assembly
962 checkpoint proteins Bub1 and BubR1. Mol Cell Biol *31*, 998-1011.
963 Krenn, V., Overlack, K., Primorac, I., van Gerwen, S., and Musacchio, A. (2014). KI motifs of human
964 Knl1 enhance assembly of comprehensive spindle checkpoint complexes around MELT repeats.
965 Curr Biol *24*, 29-39.
966 Krenn, V., Wehenkel, A., Li, X., Santaguida, S., and Musacchio, A. (2012). Structural analysis
967 reveals features of the spindle checkpoint kinase Bub1-kinetochore subunit Knl1 interaction. J
968 Cell Biol *196*, 451-467.

969 Lara-Gonzalez, P., Kim, T., Oegema, K., Corbett, K., and Desai, A. (2021). A tripartite mechanism
970 catalyzes Mad2-Cdc20 assembly at unattached kinetochores. Science *371*, 64-67.
971 Leontiou, I., London, N., May, K.M., Ma, Y., Grzesiak, L., Medina-Pritchard, B., Amin, P.,
972 Jeyaprakash, A.A., Biggins, S., and Hardwick, K.G. (2019). The Bub1-TPR Domain Interacts Directly
973 with Mad3 to Generate Robust Spindle Checkpoint Arrest. Curr Biol *29*, 2407-2414 e2407.
974 Musacchio, A. (2015). The Molecular Biology of Spindle Assembly Checkpoint Signaling Dynamics.
975 Curr Biol *25*, R1002-1018.
976 Nijenhuis, W., Vallardi, G., Teixeira, A., Kops, G.J., and Saurin, A.T. (2014). Negative feedback at
977 kinetochores underlies a responsive spindle checkpoint signal. Nat Cell Biol *16*, 1257-1264.
978 Nijenhuis, W., von Castelmur, E., Littler, D., De Marco, V., Tromer, E., Vleugel, M., van Osch, M.H.,
979 Snel, B., Perrakis, A., and Kops, G.J. (2013). A TPR domain-containing N-terminal module of MPS1
980 is required for its kinetochore localization by Aurora B. J Cell Biol *201*, 217-231.
981 Overlack, K., Bange, T., Weissmann, F., Faesen, A.C., Maffini, S., Primorac, I., Muller, F., Peters,
982 J.M., and Musacchio, A. (2017). BubR1 Promotes Bub3-Dependent APC/C Inhibition during
983 Spindle Assembly Checkpoint Signaling. Curr Biol *27*, 2915-2927 e2917.
984 Overlack, K., Primorac, I., Vleugel, M., Krenn, V., Maffini, S., Hoffmann, I., Kops, G.J., and
985 Musacchio, A. (2015). A molecular basis for the differential roles of Bub1 and BubR1 in the spindle
986 assembly checkpoint. Elife *4*, e05269.
987 Piano, V., Alex, A., Stege, P., Maffini, S., Stoppiello, G.A., Huis In 't Veld, P.J., Vetter, I.R., and
988 Musacchio, A. (2021). CDC20 assists its catalytic incorporation in the mitotic checkpoint complex.
989 Science *371*, 67-71.
990 Primorac, I., Weir, J.R., Chiroli, E., Gross, F., Hoffmann, I., van Gerwen, S., Ciliberto, A., and
991 Musacchio, A. (2013). Bub3 reads phosphorylated MELT repeats to promote spindle assembly
992 checkpoint signaling. Elife *2*, e01030.
993 Qian, J., Garcia-Gimeno, M.A., Beullens, M., Manzione, M.G., Van der Hoeven, G., Igual, J.C.,
994 Heredia, M., Sanz, P., Gelens, L., and Bollen, M. (2017). An Attachment-Independent Biochemical
995 Timer of the Spindle Assembly Checkpoint. Mol Cell *68*, 715-730 e715.
996 Roy, B., Han, S.J.Y., Fontan, A.N., and Joglekar, A.P. (2020). The copy-number and varied strength
997 of MELT motifs in Spc105 balance the strength and responsiveness of the Spindle Assembly
998 Checkpoint. Elife *9*.
999 Roy, B., Han, S.J.Y., Fontan, A.N., and Joglekar, A.P. (2021). Aurora B phosphorylates Bub1 to
1000 promote spindle assembly checkpoint signaling. bioRxiv, 2021.2001.2005.425459.
1001 Saurin, A.T., van der Waal, M.S., Medema, R.H., Lens, S.M., and Kops, G.J. (2011). Aurora B
1002 potentiates Mps1 activation to ensure rapid checkpoint establishment at the onset of mitosis.
1003 Nat Commun *2*, 316.
1004 Silio, V., McAinsh, A.D., and Millar, J.B. (2015). KNL1-Bubs and RZZ Provide Two Separable
1005 Pathways for Checkpoint Activation at Human Kinetochores. Dev Cell *35*, 600-613.
1006 Sullivan, M., Higuchi, T., Katis, V.L., and Uhlmann, F. (2004). Cdc14 phosphatase induces rDNA
1007 condensation and resolves cohesin-independent cohesion during budding yeast anaphase. Cell
1008 *117*, 471-482.
1009 Taylor, S.S., Hussein, D., Wang, Y., Elderkin, S., and Morrow, C.J. (2001). Kinetochore localisation
1010 and phosphorylation of the mitotic checkpoint components Bub1 and BubR1 are differentially
1011 regulated by spindle events in human cells. J Cell Sci *114*, 4385-4395.

1012 Vleugel, M., Omerzu, M., Groenewold, V., Hadders, M.A., Lens, S.M., and Kops, G.J. (2015).
1013 Sequential multisite phospho-regulation of KNL1-BUB3 interfaces at mitotic kinetochores. Mol
1014 Cell *57*, 824-835.
1015 Vleugel, M., Tromer, E., Omerzu, M., Groenewold, V., Nijenhuis, W., Snel, B., and Kops, G.J.
1016 (2013). Arrayed BUB recruitment modules in the kinetochore scaffold KNL1 promote accurate
1017 chromosome segregation. J Cell Biol *203*, 943-955.
1018 Yuan, I., Leontiou, I., Amin, P., May, K.M., Soper Ni Chafraidh, S., Zlamalova, E., and Hardwick,
1019 K.G. (2017). Generation of a Spindle Checkpoint Arrest from Synthetic Signaling Assemblies. Curr
1020 Biol *27*, 137-143.
1021 Zhang, G., Lischetti, T., Hayward, D.G., and Nilsson, J. (2015). Distinct domains in Bub1 localize
1022 RZZ and BubR1 to kinetochores to regulate the checkpoint. Nat Commun *6*, 7162.
1023 Zhang, G., Lischetti, T., and Nilsson, J. (2014). A minimal number of MELT repeats supports all the
1024 functions of KNL1 in chromosome segregation. J Cell Sci *127*, 871-884.
1025 Zhang, G., Mendez, B.L., Sedgwick, G.G., and Nilsson, J. (2016). Two functionally distinct
1026 kinetochore pools of BubR1 ensure accurate chromosome segregation. Nat Commun *7*, 12256.
1027